Parameter uncertainty and noise effects on the global dynamics of an electrically actuated microarch

(Article begins on next page)

23 November 2024

Parameter uncertainty and noise effects on the global dynamics of an electrically actuated microarch

Parameter uncertainty and noise effects on the global dynamics of an electrically actuated microarch

Kaio C. B. Benedetti[1], Paulo B. Gonçalves[1], Stefano Lenci[2] and Giuseppe Rega[3]

[1] Department of Civil and Environmental Engineering, Pontifical Catholic University of Rio de Janeiro, Rio de Janeiro, Brazil

[2] Department of Civil and Building Engineering, and Architecture, Polytechnic University of Marche, Ancona, Italy

[3] Department of Structural and Geotechnical Engineering, University of Rome La Sapienza, Rome, Italy

E-mail: giuseppe.rega@uniroma1.it

Abstract

This work aims to study the effect of uncertainties and noise on the nonlinear global dynamics of a micro-electro-mechanical arch obtained from an imperfect microbeam under an axial load and electric excitation. An adaptative phase-space discretization strategy based on an operator approach is proposed. The Ulam method, a classical discretization of flows in phase-space, is extended here to nondeterministic cases. A unified description is formulated based on the Perron-Frobenius, Koopman, and Foias linear operators. Also, a procedure to obtain global structures in the mean sense of systems with parametric uncertainties is presented. The stochastic basins of attraction and attractors' distributions replace the usual basin and attractor concepts. For parameter uncertainty cases, the phase-space is augmented with the corresponding probability space. The microarch is assumed to be shallow and modelled using a nonlinear Bernoulli-Euler beam theory and is discretized by the Galerkin method using as interpolating function the linear vibration modes. Then, from the discretized multi degree of freedom model (mdof) model, an accurate single degree of freedom (sdof) reduced order model, based on theory of nonlinear normal modes, is derived. Several competing attractors are observed, leading to different (acceptable or unacceptable) behaviours. Extensive numerical simulations are performed to investigate the effect of noise and uncertainties on the coexisting basins of attraction, attractors' distributions, and basins boundaries. The appearance and disappearance of attractors and stochastic bifurcation are observed, and the time-dependency of stochastic responses is demonstrated, with long-transients influencing global behaviour. To consider uncertainties and noise in design, a dynamic integrity measure is proposed via curves of constant probability, which give quantitative information about the changes in structural safety. For each attractor, the basin robustness as a function of a stochastic parameter is investigated. The weighted basin area can quantify the integrity of nondeterministic cases, being also the most natural generalization of the global integrity measure. While referring to particular MEMS, the relevance of the dynamical integrity analysis for stochastic systems to quantify tolerances and safety margins is underlined here.

1. Introduction

Micro-electro-mechanical systems, or MEMS, have been attracting a large amount of attention over the last decades due to their potential for applications in a large variety of fields such as aerospace, mechanics, electricity, communications, bioengineering and medicine. They have many functions, including transducers, switches, logic gates, actuators, and sensors. This issue is challenging since the problem is inherently multiphysical, demanding a multi-disciplinary perspective for the modelling, analysis and synthesis [1–5]. MEMS are often constituted by standard structural elements such as (micro)beams, (micro)plates and micro(arches) suspended over a parallel ground plate, and under direct current (DC) voltage, alternating current (AC) voltage, or both, and classical theories usually apply [6]. Recent review papers present the current stage of research on electrically actuated MEMS, analysing their theoretical developments and mathematical modelling, nonlinear static and dynamic behaviours, advances in fabrication technologies, development of high-performance nano and microscale systems, and other recent advances in the field [7–12].

Microarches are among the most used MEMS structures [13]. Arches are compliant bistable mechanisms having two stable equilibrium configurations and a double well potential function. The microarch configuration can be obtained by using a buckled beam or can be deliberately pre-shaped during fabrication, with bistable beams with buckled-like shapes being the most common type. The buckling can be obtained by axial compression, heating expansion, or residual stresses. Both configurations are increasingly used as bistable mechanisms at the small and large scale [14,15]. Examples of applications include soft robotics, metamaterials, multistable positioning, resonators, actuators, gas sensing, pressure sensing, threshold sensing, space applications, biomedical devices, and energy harvesting, as mentioned by Hussein et al. [16].

Many research studies highlight that, thanks to the presence of both electric and geometric nonlinearities, MEMS exhibit strongly nonlinear behaviour, and various nonlinear static and dynamic phenomena may arise in these microstructures. Thus, understanding their nonlinear dynamical behaviour is crucial for successful implementation. Among these phenomena, the pull-in, i.e., the contact of the microstructure with the charged substrate, is an inherently nonlinear and crucial effect, which may be an undesirable feature or a desirable one, depending on the application. Under alternating current (AC) voltage, the microarch may exhibit several coexisting attractors due to local or global bifurcations, the presence of multiple potential wells, and pull-in [17–20]. Thus, the set of initial conditions converging to a given attractor becomes an important design issue, and the analysis of the evolution of the coexisting basins of attraction is the basic tool for evaluating the microstructure

dynamical integrity and load-carrying capacity. The basins' topology can vary remarkably with a varying parameter, with their boundaries being smooth or fractal, depending on the stable invariant manifolds of the saddles lying on them. Furthermore, the complexity of the interwoven basins of attraction increases with the number of coexisting solutions. In such cases, responses become extremely sensitive to any perturbation, with the final state depending crucially on the initial conditions. The importance of the global dynamic analysis and dynamical integrity concept for engineering design and system safety has been clearly stated in recent contributions on macro- to nano-mechanics [17–24]. In particular, this analysis can identify the parameter range where each attractor can be reliably detected in practice and where, instead, it becomes susceptible to unknown parameter changes.

The aforementioned studies emphasize the importance of accurately predicting the nonlinear dynamic behavior of MEMS. However, this is a challenging problem due to their inherently multiphysical nature, the presence of intrinsically nonlinear electric excitation, geometrical nonlinearities, the uncertainties in the damping estimation, imperfections coming from the microfabrication process and the noise of the current, resulting in many unknown and uncertain parameters. Thus, the deterministic framework represents a theoretical limit, which may not occur in practice. A realistic analysis must include the effect of noise, uncertainties, and disturbances, which are unavoidable and may lead to an outcome different from that theoretically predicted. For example, Vig and Kim [25] enumerate possible noise sources with thermal, chemical, and electrical origins, intensifying dynamic effects that are negligible in macro-scale devices. Experimental observations [26–28] demonstrate these noise sources and their effects. Another type of nondeterminism occurs in MEMS due to possible geometric [29–31], constitutive [32], damping [33], and general [34] uncertainties. Monte Carlo based methodologies, stochastic perturbation, and stochastic collocation can be applied to the analysis. Recently, a MEM cantilever was analyzed, showing the effects of imperfection uncertainty on the frequency responses, and noise on the nonlinear global dynamics [35].

The nonlinear global dynamic analysis is computationally demanding, with many phase-space discretization techniques devoted to this problem, starting from the Ulam method [36] and later the generalized cell-mapping method [37,38]. They are actually equivalent [39] for being based on an operator perspective of global dynamics. Today, real engineering problems demand high-performance computing (HPC), with parallel strategies being essential [40–42]. Also, nondeterministic considerations add another complication, being even more computationally expensive. Orlando et al. [43] and Silva and Gonçalves [44] demonstrated this, flagging regions susceptible to nondeterministic factors through Monte

Carlo method. Basins of attraction were highly affected for large uncertainty levels, and the computational cost increased significantly with them. To reduce this cost, adaptative phase-space discretization techniques, designed for nondeterministic global dynamic analysis, are an interesting field of investigation [45]. Some recent results quantified the effects of random parameters and noise on the basins, attractors, and dynamic integrity of nonlinear one degree of freedom (dof) oscillators [46], obtained by applying an operator perspective for the nondeterministic analysis.

The formulation of reduced order models (ROMs) contributes substantially to reducing the computational cost of analysis. Younis et al. [47] proposed the construction of ROMs by multiplying the equation of motion by the electric load denominator. Many systems were analyzed following this strategy, such as arch resonators [28,29,48–50], arches over flexible supports [51], functionally graded viscoelastic microbeams with imperfections [52], cantilever resonators [53–55], narrow microbeams subject to fringing fields [56–58] and microscale beams described by the modified couple stress theory [30–32,59–63].

The derivation of reliable ROMs) has received considerable attention in recent years, especially in the analysis of nonlinear systems [64]. A recent literature review by Mazzilli et al. [65] showed that ROMs obtained through nonlinear modes are significantly superior to those provided by the classical Galerkin method. They can represent dynamics restricted to specific nonlinear manifolds with a small number of dof, a characteristic that profoundly helps the global dynamic analysis. In the MEMS literature, the works of Ruzziconi et al. [28,49] demonstrated how simple, single degree of freedom (sdof) or two degrees of freedom (2dof) systems, are capable of representing complex dynamics, comparing the Galerkin method to Ritz with Padé approximations.

The objective of this work is to study the global nonlinear dynamics of a microarch electrically actuated and to verify the effects of noise and uncertain damping ratio on global response. The mechanical model is based on [28], and is a MEMS device consisting of a shallow arched microbeam, with axial load deliberately added and electrostatic and electrodynamic actuation. The microstructure is characterized by a bistable static configuration [66], with complex global dynamics. A ROM is derived for the analysis of the pre-buckling potential well, and the modified adaptative phase-space discretization strategy presented in [46] is employed for the global dynamic analysis. This methodology allows the effects of noise and uncertain parameters to be highlighted.

The paper is organized as follows. Section 2 presents the MEMS formulation and discretization procedure. The static analysis and investigation of the minimum number of linear modes needed in the Galerkin procedure are presented in section 3. In section 4, the ROM embedded in a lower

dimensional invariant manifold [65] is derived, using the theory of nonlinear normal modes. The frequency response analyses of both the ROM and a 2dof Galerkin model are compared in section 5. In section 6, the global analysis of the deterministic arch is presented. The influence of noise and damping uncertainty is investigated in, respectively, section 7.1, and section 7.2. Section 8 presents the concluding remarks.

2. Nonlinear Euler-Bernoulli microarch electrically actuated

A micro-electro-mechanical system model is derived based on the experimental and numerical analyses in [28]. The microstructure is simulated as a clamped-clamped imperfect planar Euler-Bernoulli microbeam [67], with length L and a constant rectangular cross-section of width b and thickness h. As in [28], residual stresses are represented by a constant axial load P, which produces the axial displacement u_B at the right end of the beam. Three coordinate systems are considered, the reference system (X, Z), the undeformed, stress-free configuration (ξ_0, ζ_0), and the deformed configuration (ξ, ζ) [35]. The transversal imperfection w_0 and displacement w are related through these coordinate systems, from which the equations of motion are derived. Both undeformed and deformed configurations and the reference system are shown in Figure 1. The actuation plate is also depicted at a positive distance d in the adopted reference system.

The Euler angles θ and θ_0, and the arclength definitions $\tilde{s}$ and s are also shown in Figure 1. Based on the Euler beam theory, the axial strain is given by

$$\varepsilon_{\xi\xi} = \Delta_e + \zeta\left(\bar{\theta}' - \theta_0'\right), \tag{1}$$

where $\bar{\theta} = \theta + \theta_0$, $()' = \frac{d}{ds}$ is the derivative with respect to the undeformed arclength s, and Δ_e is the axial elongation,

$$\Delta_e = \sqrt{\left(u' + \sqrt{1 - w_0'^2}\right)^2 + \bar{w}'^2} - 1. \tag{2}$$

Through geometry, the following relations are obtained [46,67]

$$\sin\bar{\theta} = \frac{-\bar{w}'}{\sqrt{\bar{w}'^2 + \left(u' + \sqrt{1 - w_0'^2}\right)^2}},$$

$$\cos\bar{\theta} = \frac{u' + \sqrt{1 - w_0'^2}}{\sqrt{\bar{w}'^2 + \left(u' + \sqrt{1 - w_0'^2}\right)^2}}, \tag{3}$$

$$\sin\theta_0 = -w_0', \qquad \cos\theta_0 = \sqrt{1 - w_0'^2},$$

where $\bar{w} = w + w_0$. Finally, the Lagrangian is defined as $\mathsf{L} = T - U$, where the kinetic energy is given by

$$T = \frac{1}{2}\int_S \left\{ m\dot{u}^2 + m\dot{w}^2 \right\} ds, \tag{4}$$

and the strain potential energy is

$$U = \frac{1}{2}\int_S \left\{ D_u \Delta_e{}^2 + D_\eta \theta'^2 \right\} ds, \tag{5}$$

where m is the linearly distributed mass, $(\,)^\square = \frac{d}{dt}$, and $D_u = EA$ and $D_\eta = EJ$ are the axial and flexural stiffnesses, E being the Young's modulus, A the cross-section area and J the cross-section area moment of inertia.

The equations of motion are derived by applying Hamilton's principle, that is, by taking $\mathsf{H} = \mathsf{L} + W_{nc}$ as stationary in time, where $\delta W_{nc} = (Q_w - c_w \dot{w})\delta w$ are the nonconservative forces, resulting in:

$$m\ddot{u} = \left\{ D_u \left(u' + w'w_0' + \frac{w'^2}{2} \right) + D_\eta \bar{w}'w''' \right\}', \tag{6}$$

$$\begin{aligned}
m\ddot{w} + c_w \dot{w} - Q_w &= \left\{ D_u \bar{w}' \left(u' + w'w_0' + \frac{w'^2}{2} \right) \right. \\
&\quad + D_\eta \left[\left(w_0'''w' + 2(\bar{w}'w'')' \right)\bar{w}' - w'''\left(w_0'^2 + 1 \right) \right. \\
&\quad \left. \left. + w'w_0''(\bar{w}'' + w'') + u'w''' + (u'\bar{w}')'' \right] \right\}'.
\end{aligned} \tag{7}$$

Following Nayfeh and Pai [67], the effects of the geometric nonlinearities related to the curvature and axial shortening of the microbeam up to third order are retained in equation (7).

Taking u as time-independent, integrating equation (6) twice with respect to s and applying boundary conditions $u(0) = 0$ and $u(L) = -u_B$ results in

$$\begin{aligned}
u &= \frac{s}{L}\int_0^L \left\{ w'\left(\frac{w'}{2} + w_0' \right) + \frac{D_\eta}{D_u}\bar{w}'w''' \right\} ds - \frac{s}{L}u_B \\
&\quad - \int_0^s \left\{ w'\left(\frac{w'}{2} + w_0' \right) + \frac{D_\eta}{D_u}\bar{w}'w''' \right\} ds.
\end{aligned} \tag{8}$$

Only the initial displacement w_0 is stress-free. The boundary condition u_B imposes an initial deformation that is not in equilibrium. Thus, the corresponding w must be calculated.

Considering a parallel plate capacitor with a rectangular cross-section, the electrostatic force Q_w can be written as [2]

$$Q_w = \frac{b\varepsilon V^2}{2(d - \bar{w})^2}, \tag{9}$$

where b is the beam width, d is the initial gap for a perfect system, ε is the free space permittivity and V is the applied voltage.

Finally, by considering the following nondimensional parameters

$$\begin{aligned}
s^* &= \frac{s}{L}, \quad t^* = t\sqrt{\frac{D_\eta}{mL^4}}, \\
w^* &= \frac{w}{d}, \quad w_0^* = \frac{w_0}{d}, \quad u_B^* = \frac{u_B}{L}, \\
Q_w^* &= \frac{Q_w L^3}{D_\eta}, \quad \beta_u^* = \frac{D_u L^2}{D_\eta}, \\
c_w^* &= \frac{c_w L^2}{\sqrt{mD_\eta}}, \quad \varepsilon^* = \varepsilon\frac{L^2}{D_\eta}, \\
d^* &= \frac{d}{L}, \quad b^* = \frac{b}{L},
\end{aligned} \tag{10}$$

the nondimensional equation of motion in the transversal direction is obtained as

$$\begin{aligned}
&\ddot{w} + c_w\dot{w} + w^{iv} + \beta_u\bar{w}''\left\{ u_B - d^2\int_0^1 \left(\frac{w'^2}{2} + w'w_0' \right) ds \right\} \\
&- \frac{b\varepsilon V^2}{2d^3(1-\bar{w})^2} = \left[\bar{w}'' + \frac{d^2}{\beta_u}\left(w^{iv} + \bar{w}^{iv} \right) \right]\int_0^1 \bar{w}'w''' ds \\
&- \left(w^{iv} + \bar{w}^{iv} \right)\left\{ u_B - d^2\int_0^1 \left(\frac{w'^2}{2} + w'w_0' \right) ds \right\} \\
&- \left\{ d^2\left[w'\left(\frac{w'w_0'''}{2} + w_0''^2 + (w_0'w_0'')' \right) \right. \right. \\
&\quad \left. + \bar{w}'\left(w''w_0'' + (w''\bar{w}')' \right) \right] \\
&\quad \left. + \frac{d^2}{\beta_u}\left[(\bar{w}'^2 w''')'' - \bar{w}'w'''^2 \right] \right\}'.
\end{aligned} \tag{11}$$

where $*$ was dropped for brevity. With respect to the condensed microbeam model used in [28], the r.h.s. of Eq. (11) is different from zero due to the nonlinearities being considered.

The initial configuration is assumed in the form of the clamped-clamped beam buckling mode [28], which, in nondimensional form, is given as

$$w_0^* = \frac{y_0^*}{2}\left(1 - \cos(2\pi s) \right), \tag{12}$$

where y_0^* is the maximum initial rise of the imperfect beam at $s^* = 0.5$, nondimensionalized with respect to the nominal beam gap *d*. Thus, $y_0^* = 1$ corresponds to a pull-in failure and is an inadmissible parameter value. The linear vibration modes of the clamped-clamped Euler-Bernoulli beam [46,68]

$$F_i(s) = C_i \left\{ \cosh\left(\sqrt{\omega} s\right) - \cos\left(\sqrt{\omega} s\right) + \frac{\sin\sqrt{\omega} + \sinh\sqrt{\omega}}{\cos\sqrt{\omega} - \cosh\sqrt{\omega}} \left[\sinh\left(\sqrt{\omega} s\right) - \sin\left(\sqrt{\omega} s\right) \right] \right\}, \quad (13)$$

are adopted in the Galerkin discretization and the natural frequencies are the nontrivial solutions of the characteristic equation $\cos\sqrt{\omega} \cosh\sqrt{\omega} = 1$.

The present formulation is valid for shallow arches under small to moderate displacements. Also, the capacitor assumption [2] dictates that the system behaves as parallel plates. The parameters of Ruzziconi et al. [28] consider these constraints and are adopted in this study, with the dimensional values summarized in Table 1.

Table 1. Dimensional geometric and material properties

Parameters	Symbol	Values
Length (μm)	*L*	440
Width (μm)	*b*	55.8
Thickness (μm)	*h*	1.864
Linear mass distribution (kg/m)	*m*	2.4255×10^{-7}
Flexural stiffness (N·μm²)	D_η	4.9992
Axial stiffness (N)	D_u	17.2659
Nominal gap (μm)	*d*	0.7
Free space permittivity (N·V⁻²) [69]	ε	8.85×10^{-12}
Initial transversal displacement at $s = 0.5L$ (μm)	y_0	-1.347
Axial displacement at $s = L$ (μm)	u_B	0.0296

The corresponding nondimensional parameters, given by equation (10), are reported in Table 2. Only the free space permittivity ε^* still maintains a dimension unit, V⁻², as usually done in the literature. This choice simplifies the presentation of the results, with both the direct current V_{dc} and alternate current V_{ac} components of the load *V* in (11) given in units of Volt (V).

Table 2. Nondimensional geometric and material parameters

Parameters	Symbol	Values
Width	b^*	0.1268
Nominal gap	d^*	0.0016
Free space permittivity (V⁻²)	ε^*	3.4273×10^{-7}
Axial stiffness	β_u^*	668643.74
Initial transversal displacement at $s^* = 0.5$	y_0^*	-1.9243
Axial displacement at $s^* = 1$	u_B^*	6.7288×10^{-5}

The minus sign of y_0 and y_0^* results from the axis orientation being negative upwards, which implies a total initial gap larger than the nominal gap: in dimensional form, the maximum initial gap is $|y_0| + d = 2.047 \mu m$. The nondimensionalization of the displacement field in [28] is with respect to a nominal micrometer, while here the nominal gap *d* is adopted. Thus, the pull-in position becomes $w = 1$, represented by the pole of equation (11). In the following sections, the nondimensional formulation is considered and the symbol * is dropped for brevity, unless stated otherwise.

3. Equilibrium at static actuation

The total applied voltage is the sum of the direct current (V_{dc}) and the time-dependent alternate current (V_{ac}), i.e.,

$$V(t) = V_{dc} + V_{ac}(t). \quad (14)$$

The transversal displacement is, therefore, decomposed into its dynamic and static parts,

$$w(t,x) = w_d(t,x) + w_s(x). \quad (15)$$

The static response of the microarch is now investigated. Initially, the modal equations are obtained. Following a classical procedure [2], equation (11) is multiplied by the load denominator, $(1-\bar{w})^2$, the time dependent terms are deleted, and then a Galerkin projection using the linear vibration modes, equation (13), is conducted, resulting in the following system of nonlinear equilibrium equations

$$\begin{aligned} w_i &\left[\mathbf{B}_{in} - w_j \mathbf{B}_{ijn} + w_j w_k \mathbf{B}_{ijkn} \right] + \beta_u \left(\mathbf{C}_n + w_i \mathbf{C}_{in} \right. \\ &+ w_i w_j \mathbf{C}_{ijn} + w_i w_j w_k \mathbf{C}_{ijkn} + w_i w_j w_k w_l \mathbf{C}_{ijkln} \\ &\left. + w_i w_j w_k w_l w_m \mathbf{C}_{ijklmn} \right) = \mathbf{D}_n + w_i \mathbf{D}_{in} + w_i w_j \mathbf{D}_{ijn} \\ &+ w_i w_j w_k \mathbf{D}_{ijkn} + w_i w_j w_k w_l \mathbf{D}_{ijkln} \\ &+ w_i w_j w_k w_l w_m \mathbf{D}_{ijklmn} + \frac{b \varepsilon V_{dc}^2}{2d^3} \int_0^1 F_n \, ds, \end{aligned} \quad (16)$$

where w_i are the static modal amplitudes, the tensor constants are given in Appendix A, and the Einstein summation convention is adopted, with indexes i, j, k, l, m, n varying from 1 to the total number of linear vibration modes, equation (13), adopted in the Galerkin discretization procedure. Equation (16) presents nonlinearities up to the fifth order with coupling between all linear modes. The nonlinear equilibrium paths are obtained through a pseudo arc-length continuation procedure together with the Newton-Raphson method [70,71], and their stability is verified through the maximum eigenvalue of the Jacobian matrix.

AUTHOR SUBMITTED MANUSCRIPT - JMM-106059.R2   Page 6 of 29

J. Micromech. Microeng. **XX** (XXXX) XXXXXX   Benedetti *et al*

The static equilibrium responses for various imperfection levels are displayed in Figure 2, considering an increasing number of modes, namely, the first, third and fifth linear symmetric modes, that is, i,j,k,l,m,n can be $\{1\}$, $\{1,3\}$, or $\{1,3,5\}$. The vertical axis corresponds to the total static displacement $\bar{w}_s$ at the middle of the microarch span, $s = 0.5$, with respect to the perfect reference system. That is, it accounts for the displacement due to the static actuation V_{dc}, the initial imperfection y_0, and the initial axial displacement u_B. Recalling the nondimensional relations in (10), the case $\bar{w}_s^*(0.5) = 1$ corresponds to pull-in.

At least the first two symmetric modes are necessary to predict with precision the nonlinear response before pull-in for all imperfection levels and, consequently, the associated potential energy function and the ensuing global dynamics. For $y_0 \geq -2$, the results indicate the viability of the 2-mode expansion for shallow arches, being a good compromise between quality of results and difficulty of analysis [46]. Notice that, although the imperfection magnitude y_0 is a multiple of the nominal gap d, it is still very small in comparison to the nominal microarch span L [28]. The maximum absolute displacement corresponds to 0.477% of the microarch span for $y_0 = -2$. Therefore, the displacements are still very small. Finally, symmetry-breaking bifurcations are not considered, so asymmetric modes are not included in the analysis.

4. Reduced order model based on nonlinear normal modes

Here the concept of normal nonlinear modes is used to derive a reliable sdof ROM for the microarch [65]. The usual procedure to obtain the modal equations of motion is to define the displacement w as a sum of static and dynamic components, equation (15), expand the dynamic part in Taylor series, and then apply a Galerkin projection onto the linear vibration modes [2]. The resulting nonlinear system represents a dynamic perturbation of the static position. Depending on the excitation frequency and the expected displacement amplitude, several linear modes are necessary to describe the original continuous problem correctly [72]. This is a problem for global dynamic analysis since the phase-space dimension increases with the number of modal equations n (dimension 2^n), and discretization of multidimensional spaces is still computationally prohibitive, especially when noise and uncertainties are considered.

To address this issue, a reduced order model is derived. As in the static analysis, by multiplying equation (11) by $(1-\bar{w})^2$ and then applying the Galerkin projection without separating static and dynamic displacement components, the system of nonlinear equations takes the form

$$
\begin{aligned}
(\ddot{w}_i + c_w \dot{w}_i)&\left[\mathbf{A}_{in} - w_j \mathbf{A}_{ijn} + w_j w_k \mathbf{A}_{ijkn} \right] \\
&+ w_i \left[\mathbf{B}_{in} - w_j \mathbf{B}_{ijn} + w_j w_k \mathbf{B}_{ijkn} \right] + \beta_u \left(\mathbf{C}_n + w_i \mathbf{C}_{in} \right. \\
&+ w_i w_j \mathbf{C}_{ijn} + w_i w_j w_k \mathbf{C}_{ijkn} + w_i w_j w_k w_l \mathbf{C}_{ijkln} \\
&\left. + w_i w_j w_k w_l w_m \mathbf{C}_{ijklmn} \right) = \mathbf{D}_n + w_i \mathbf{D}_{in} + w_i w_j \mathbf{D}_{ijn} \\
&+ w_i w_j w_k \mathbf{D}_{ijkn} + w_i w_j w_k w_l \mathbf{D}_{ijkln} \\
&+ w_i w_j w_k w_l w_m \mathbf{D}_{ijklmn} + \frac{b\varepsilon}{2d^3}(V_{dc}+V_{ac})^2 \int_0^1 F_n \, ds,
\end{aligned} \tag{17}
$$

where the Einstein summation convention is adopted, the constant tensors are given in Appendix A, and the same indexes as in equation (16) hold. The load V is separated into static and dynamic contributions, namely the direct current voltage V_{dc} and the alternating current voltage V_{ac}. This is a strongly nonlinear equation, with second-order nonlinearities in the inertia and damping terms and nonlinear stiffness terms up to the fifth-order. Modal systems obtained from equation (17) are highly coupled, complicating the analysis.

Following the results from the static analysis, the symmetric 2-mode expansion is initially adopted, where $i,j,k,l,m,n = \{1,3\}$. However, the adoption of the 2-mode expansion results in a 4-dimensional phase-space, which is still complicated to analyse. An alternative is to restrict the analysis to solutions embedded in a lower dimensional invariant manifold [65], following the definition of nonlinear normal modes of Shaw and Pierre [72].

To construct the ROM, the 2dof system is expanded using Taylor series up to the fifth order around a static equilibrium position given by the modal amplitudes of two symmetric modes obtained by the solution of equation (16), $\left(w_s^{(1)}, w_s^{(2)}\right)$, for a given value of direct current voltage V_{dc}. The indexes (1) and (2) correspond to the first and third linear vibration modes, given by equation (13), which are also the first two symmetric modes. The resulting first-order differential system is derived

$$
\begin{aligned}
\frac{d}{dt} w_k &= \dot{w}_k, \\
\frac{d}{dt} \dot{w}_k &= F_k \left(w_s^{(1)}, w_s^{(2)}, V_{dc}, \dot{w}_1, \dot{w}_2, w_1, w_2, V_{ac} \right),
\end{aligned} \tag{18}
$$

where $k = \{1,2\}$ represent the first and second linear symmetric modes.

For the following numerical analysis, the static position is calculated assuming $V_{dc} = 0.7$V, as in [28], with parameters from Table 2, and $w_s^{(1)} = -0.8382$, $w_s^{(2)} = 0.0200$. Then, the procedure described in [72] is applied. One of the modal amplitudes and the corresponding velocity are taken as the independent manifold variables (master pair), while the others

are assumed as dependent variables (slave coordinates). Here the first modal amplitude and the corresponding velocity, w_1 and $\dot{w}_1$, are adopted as governing or master coordinates, and the second modal amplitude and velocity, w_2 and $\dot{w}_2$, as slave coordinates. Expanding the slave coordinates up to the fifth order results in

$$w_2 = a_0 + \sum_{n=1}^{5}\sum_{i=0}^{n} a_{i,n} w_1^{n-i} \dot{w}_1^{i}, \tag{19}$$

$$\dot{w}_2 = b_0 + \sum_{n=1}^{5}\sum_{i=0}^{n} b_{i,n} w_1^{n-i} \dot{w}_1^{i}. \tag{20}$$

The constants are obtained by substituting equations (19) and (20) into the first and second of equations (18), respectively, for $k = 2$, and by setting damping and forcing terms to zero. This results in a two-equation system of $\left(w_1, \dot{w}_1, \ddot{w}_1\right)$. The acceleration term $\ddot{w}_1$ is eliminated by applying the second equation in (18), with $k = 1$. Retaining terms up to the fifth power of w_1 and $\dot{w}_1$ results in the system

$$C_{1;0} + \sum_{n=1}^{5}\sum_{i=0}^{n} C_{1;i,n} w_1^{n-i} \dot{w}_1^{i} =$$

$$C_{2;0} + \sum_{n=1}^{5}\sum_{i=0}^{n} C_{2;i,n} w_1^{n-i} \dot{w}_1^{i}, \tag{21}$$

$$C_{3;0} + \sum_{n=1}^{5}\sum_{i=0}^{n} C_{3;i,n} w_1^{n-i} \dot{w}_1^{i} =$$

$$C_{4;0} + \sum_{n=1}^{5}\sum_{i=0}^{n} C_{4;i,n} w_1^{n-i} \dot{w}_1^{i}, \tag{22}$$

which are dependent on the constants $a_{i,n}$ and $b_{i,n}$ in equations (19) and (20). Terms of the same degree are equated resulting in a system of algebraic equations in terms of $a_{i,n}$ and $b_{i,n}$, which can be solved sequentially, as in any perturbation method [72]. These characteristics make it possible for the method to be easily used in computational solution schemes, even for systems with many degrees of freedom [73]. The resulting nonlinear polynomial system

$$C_{1;0} - C_{2;0} = 0,$$
$$C_{3;0} - C_{4;0} = 0,$$
$$C_{1;i,n} - C_{2;i,n} = 0, \quad \forall i,n, \tag{23}$$
$$C_{3;i,n} - C_{4;i,n} = 0, \quad \forall i,n,$$

governs the coefficients $a_{i,n}$ and $b_{i,n}$. In this case, there are forty-two equations up to the fifth power in $a_{i,n}$ and $b_{i,n}$. This approach for the approximate solution of the system of differential equations is local by nature, and results in

approximations to the nonlinear normal modes of vibration and dynamics close to the equilibrium point.

Solving this problem results in the nonlinear normal mode governed by

$$\frac{d}{dt} w_1 = \dot{w}_1,$$

$$\frac{d}{dt} \dot{w}_1 = 5.0854 w_1^5 + 14.3037 w_1^4 - 2.4554 \times 10^{-6} \dot{w}_1^4$$
$$+ 0.0035 \dot{w}_1^2 - \left(121.6181 + 0.0224 \dot{w}_1^2\right) w_1^3$$
$$+ \left(762.4990 - 0.0114 \dot{w}_1^2\right) w_1^2$$
$$- \left(1385.5761 - 0.0172 \dot{w}_1^2 + 1.5913 \times 10^{-5} \dot{w}_1^4\right) w_1. \tag{24}$$

Figure 3 illustrates the two-dimensional manifold given by equation (24), based on equations (19) and (20), embedded in a four-dimensional phase-space. This manifold is tangent to the plane corresponding to the linear normal mode at the origin, also present in the figure. The plane corresponds to the linear terms in equations (19) and (20), being a linear modal embedding of the original problem. For small $\left(w_1, \dot{w}_1, w_2, \dot{w}_2\right)$, the motion is restricted to this plane. As $\left(w_1, \dot{w}_1, w_2, \dot{w}_2\right)$ increase, nonlinear terms in equations (19) and (20) become relevant, with the two-dimensional manifold deviating from the linear solution.

By substituting equations (19) and (20) into equation (18), for $k = 1$, the first-order nonlinear equations of the forced and damped system are given by

$$\frac{d}{dt}w_1 = \dot{w}_1,$$

$$\frac{d}{dt}\dot{w}_1 = 5.0854w_1^5 + 14.3037w_1^4 - 2.4554\times10^{-6}\dot{w}_1^4$$
$$+ 0.0035\dot{w}_1^2 - \left(121.6181 + 0.0224\dot{w}_1^2\right)w_1^3$$
$$+ \left(762.4990 - 0.0114\dot{w}_1^2\right)w_1^2$$
$$- \left(1385.5761 - 0.0172\dot{w}_1^2 + 1.5913\times10^{-5}\dot{w}_1^4\right)w_1.$$
$$- c_w^{(1)}\dot{w}_1 + \left(c_w^{(1)} - c_w^{(2)}\right)\left[-0.0104w_1\dot{w}_1 - 0.1449\dot{w}\right.$$
$$+ \left(0.0351w_1^4 + 1.0034\times10^{-5}w_1^2\dot{w}_1^2\right)\dot{w}_1$$
$$+ \left(0.0164w_1^2 + 6.5676\times10^{-7}\dot{w}_1^2\right)w_1\dot{w}_1$$
$$- \left(0.0193w_1^2 - 5.2796\times10^{-6}\dot{w}_1^2\right)\dot{w}_1\left.\right]$$
$$+ V_{ac}\left[0.6280 + 1.0091\times10^{-5}w_1^2\dot{w}_1^2 + 0.0399w_1^4\right.$$
$$+ 0.0980w_1^3 + 7.2601\times10^{-6}w_1\dot{w}_1^2$$
$$+ 1.0335\times10^{-6}\dot{w}_1^2 + 0.2257w_1^2 + 0.4405w_1\left.\right]$$
$$+ V_{ac}^2\left[0.0700w_1^3 + 5.1858\times10^{-6}w_1\dot{w}_1^2\right.$$
$$+ 0.1612w_1^2 + 7.3821\times10^{-7}\dot{w}_1^2$$
$$+ 0.3146w_1 + 0.4486\left.\right],$$

(25)

which is the reduced order model for vibrations in the pre-buckling potential well, with $\left(w_1, \dot{w}_1\right) = \left(0,0\right)$ as the energy minimum.

If $c_w^{(1)} = c_w^{(2)}$, the damping is significantly simplified, which is the case adopted in [28]. Here, the damping ratio ξ is the same for the two modes, leading to distinct values for $c_w^{(1)}$ and $c_w^{(2)}$, and also to nonlinear damping terms in equation (25).

5. Frequency response under dynamic actuation

The dynamic actuation is given by the periodic voltage,

$$V_{ac} = A\cos\left(\Omega t\right),$$
(26)

where A is the forcing magnitude, and Ω is the forcing frequency. The damping coefficients are given in terms of the damping ratio, ξ, as

$$c_w^{(1)} = 2\xi\omega_1,$$
$$c_w^{(2)} = 2\xi\omega_2,$$
(27)

where ω_1 and ω_2 are the first and second natural frequencies. The natural frequencies are a function of the static voltage V_{dc}, the initial axial displacement u_B, and the initial imperfection y_0. For the parameters in Table 2 and $V_{dc} = 0.7$V, the natural frequencies are $\omega_1 = 37.6699$ and $\omega_2 = 116.7780$.

The analysis is conducted with the software Continuation Core and Toolboxes (COCO) [74]. Initially, the free vibrations of the 2dof model, described by the 2-mode expansion, equation (17), and the conservative reduced order model, equation (24), are compared. The backbone curves are shown in Figure 4 in terms of the transversal displacement $\bar{w}$ at $s = 0.5$, with respect to the reference frame, which is sum of the initial imperfection w_0, the static displacement w_s due to the direct current V_{dc}, and the dynamic displacement w_d due to the alternate current V_{dc}, being thus the real, observable displacement.

A softening behavior is observed, with both the small amplitude (nonresonant) and large amplitude (resonant) solutions coexisting in a frequency band lower than the resonant frequencies. This is due to the strong nonlinear electric load, which is known to lead to a softening behavior. Also, shallow arches such as those studied here display a softening behavior [75]. The initial rise of the shallow arch has a significant effect on reducing its hardening behavior and increasing the softening one, as shown by Younis et al. [76]. Such behavior matches the experimental results in [28], validating the present modelling strategy.

The two models agree qualitatively well in terms of transversal displacement $\bar{w}$, even for large values. The ROM and the 2dof model are compared in Figure 5 where the frequency response curves are shown for $A = 17$V, $\xi = 0.05$ and $\xi = 0.03$. Two resonance regions are observed, one at $\Omega = 37.2$ and other at $\Omega = 18.6$. The former corresponds to the first mode natural frequency, while the latter is a superharmonic resonance. The superharmonic resonance is due to the term V_{ac}^2 in both the reduced model, equation (25), and the 2dof model, equation (17). This is a well-known phenomenon in MEMS literature [77]. Specifically, the superharmonic resonance is more prominent, with larger displacement values. Markers identify the bifurcation points: saddle-node bifurcation points in green and period-doubling bifurcation points in red. Stable and unstable solutions are identified by continuous and dashed lines, respectively. The ROM agrees well with the 2dof model, including the point where the saddle-node bifurcation occurs, demonstrating the quality of the ROM as a lower dimensional substitute of the original model expansion for excitation frequencies up to the first resonance region. The impact of increasing forcing amplitude is demonstrated in Figure 6, for $\xi = 0.05$, in Figure 7, for $\xi = 0.03$, and in Figure 8, for $\xi = 0.01$. The main resonant region exhibits small amplitude vibrations for the two former cases, while the superharmonic region presents much larger vibration amplitudes. For smaller damping ratios, $\xi = 0.01$, Figure 8, a more complex response is observed, with the main resonant region exhibiting large amplitude vibrations. This shows the importance of the damping parameter on the results. Thus, the influence of damping uncertainty will be explored later in this work.

6. Deterministic global analysis

The deterministic global dynamics of the arch are now addressed through the ROM given by equation (25) with harmonic dynamic actuation, equation (26), and damping coefficients, equation (27). For consistency and suitable comparison, deterministic basins of attraction are obtained through the same adaptive phase-space discretization technique, designed for nondeterministic global dynamic analysis in the framework of the operator approach, used later in Section 7 to obtain stochastic and parametric uncertainty basins. A concise description of the discretized operator approach used here and in Sect. 7 is provided in Appendix B. A more detailed description is found in [46], where also an extensive literature review is presented. The superharmonic resonance region is investigated, considering a forcing frequency $\Omega = 15$ and an excitation amplitude $A = 17V$ in all cases. Resonant (large amplitude) and nonresonant (small amplitude) solutions are expected for these parameters, as observed in the frequency response analysis (Sect. 5), as well as an escape solution representing the pull-in (failure) of the system, The fourth order Runge-Kutta integrator is adopted, with time-step T/2000. The analyzed phase-space window is $X = \{-2,3\} \otimes \{-70,60\}$, which contains all relevant attractors.

Basins of attraction are shown in Figure 9 in terms of probability distributions (according to color bars' scale), by separately considering nonresonant, resonant and escape solutions so to not miss information about the varying probability of each basin. Changes in the basins' topology with the damping ratio ζ are apparent. For $\zeta = 0.05$, the two basins are robust, with well-defined smooth boundaries. As the damping ratio decreases, both basins' integrity degrades, with escape tongues gradually eroding them, with the resonant basin more affected than the nonresonant one. This is also evident in the probability increase of the escape region with decreasing damping ratio. Also, the resonant and the nonresonant basins become more intertwined as ζ decreases, although for $\zeta = 0.01$ they are still fairly well separated from each other by the escape basin entered in between them (see Figure 9(c)). In the nonresonant and resonant basins of Figure 9 there are localized regions along the boundaries, far from the attractors, with probability between 0 and 1. This is due to a smoothing resulting from the operator approach, which causes small numerical diffusion along classical deterministic boundaries. According to Ulam [36], in the limit of infinity resolution, the method converges to the expected sharp boundaries.

The efficiency of the adopted hierarchical procedure of phase-space refinement [46] is compared against that of a uniformly discretized phase-space, both strategies using the same minimum cell size and, therefore, providing the same attractors and basins results. The adaptive discretization

algorithm reduced the total number of integrated initial conditions and the total number of cells by at least 30% and 60%, respectively. Higher economy values were observed in [46] for simpler phase-space structures, which is an expected outcome.

As an example, Figure 10 shows a phase-space final discretization by applying the adaptive algorithm described in [45,46]. Some regions, particularly attractors and basins boundaries, after several interactions, have a much higher box-resolution. The adaptive discretization reduces the analysis' computational cost without losing precision in these important regions. This economy is expected to be greater if the important regions are localized in small phase-space areas, as showed in [45,46].

7. Nondeterministic global analysis

The framework for the analysis of nondeterministic dynamics though an operator approach has been addressed recently in [45,46], see also Appendix B. There, pairs of dual global operators, each pair constituted by a transfer and a composition operator, are employed for each type of dynamical system. The transfer operators for deterministic, stochastic, and parametric uncertainty cases are, respectively, the Perron-Frobenius P_t, the Foias F_t, and the parameter indexed Perron-Frobenius $P_t(\lambda)$ operators. The composition operators are for all cases Koopman K_t operators. They are discretized through the Ulam method [36], a classical discretization of flows in phase-space, which is extended here to nondeterministic cases. In [46] Benedetti proposes two strategies for phase-space discretization and refinement. The first strategy is based on a heuristic boundary identification procedure, where the basin boundary cells are cyclically subdivided using a binary tree structure. The second approach, used here, is based on the identification of the saddles' stable manifolds, which are related to the basin boundaries' geometry. All phase-space dimensions are subdivided simultaneously using an r-tree structure, thus reducing the number of initial conditions and the cost of high dimensional problems. A concise description of the construction of the discretized operators and the information given by them is provided in Appendix B.

7.1 Effects of additive white noise

On one hand, almost all theoretical and most numerical studies of nonlinear dynamics are performed for idealized noise-free systems; on the other hand, in experiments and real-life, noise is ubiquitous. Here, a white noise is represented by the generalized derivative of the standard Wiener process, $\sigma \dot{W}$, where σ is a scaling parameter. It is added to the right side of the second equation of the ROM, equation (25), and

considering the harmonic dynamic excitation, equation (26), and damping, equation (27), results in a stochastic differential system of Itô type. The sampling numerical integration of this system is obtained by a stochastic Runge-Kutta method of fourth order in drift and half order in diffusion, with the same time-step of the deterministic case, $T/2000$. Ten samples for each set of initial conditions are integrated for the construction of the discretized Foias operator $p_{ij} \approx F_h$.

The effect of noise on the attractors and basins is investigated, and the results are displayed in Figure 11, for the nonresonant attractor, and in Figure 12, for the resonant attractor. A damping ratio $\xi = 0.03$ is adopted in this section. As Lindner and Hellmann [78] discussed, the generalization of stochastic basins of attraction for noisy dynamical systems, which assigns to each phase-space region a probability of converging to a specific attractor, given a fixed time-horizon, $1/\varepsilon$, is adopted. In all cases, the time-horizon for the stochastic basin computation in equation (B3) [46] is $1/\varepsilon = 10^9 T$, giving the expected outcome. For $\sigma = 0.5$, see Figure 11(a) and Figure 12(a), the basins' boundaries maintain the same structure as in the deterministic case, but a slight diffusion is already evident, with regions with a probability between 0 and 1 appearing. These regions are here referred to as nondeterministic. Also, the noise results in the mild spreading of both attractors over the phase-space, with the resonant attractor seemingly more sensitive to it. As noise increases up to $\sigma = 1.4$, these effects increase, the attractors spreading over larger regions of phase-space and basin boundaries becoming more diffused, Figure 11(c) and 12(c). The distance between the resonant attractor and its basin's boundary decreases considerably, indicating a loss of dynamic integrity for this system. For $\sigma \geq 1.6$, only the nonresonant attractor is observed. The previous resonant basin becomes nondeterministic, being partially absorbed by the nonresonant basin: initial conditions in this region have a probability between 40% and 50% to converge to the nonresonant attractor after 10^9 periods of excitation, and the complementary probability corresponds to escape. The stochastic basin's change for $\sigma \geq 1.6$ is akin to a global bifurcation, drastically changing the outcome for this system. This stochastic erosion is correlated to the noise influence onto the hilltop saddle's manifolds, see [46]. This will be a topic for future investigations.

The nonautonomous character of stochastic dynamical systems suggests that stochastic basins are time dependent. An investigation of the transient behavior is desirable for $\sigma \geq 1.6$, when the resonant attractor disappears. To this end, the transient behavior for $\sigma = 1.6$ is addressed. Increasing values of the time-horizon $1/\varepsilon$ are considered in equation (B3) [46], with the function id_A marking the nonresonant or resonant attractor, or the escape solution. The results for $\sigma = 1.6$ are summarized in Figure 13, for the nonresonant attractor, in Figure 14, for the resonant attractor, and in Figure 15, for the escape solution. Similar results are obtained for sigma $\sigma = 1.8$

and $\sigma = 2.0$. The first three time-horizons, with $\varepsilon = 0.5$, $\varepsilon = 0.1$, and $\varepsilon = 0.01$, show the transient stochastic basin spreading in phase space but already with regions of probability lower than one, see Figures 13(a, b, c), 14(a, b, c), and 15(a, b, c). The resonant basin starts to decrease for $\varepsilon \leq 10^{-7}$, that is, after 10^7 periods of excitation. This is demonstrated in Figure 14(d, e), for $\varepsilon = 10^{-7}$ and $\varepsilon = 10^{-8}$. For $\varepsilon = 10^{-9}$, Figure 14(f), the resonant basin completely disappears, with initial conditions in this region converging either to the nonresonant basin or to the escape region. These results stress the time dependency of basins in stochastic systems. Due to computational limitations, the system is assumed ergodic for $1/\varepsilon \geq 10^9$, that is, it has converged to the steady-state response after 10^9 periods of excitation.

The integrity measure proposed in [46] is applied to quantify the system's integrity loss due to nondeterministic effects. It is defined as the weighted normalized basins' areas,

$$\frac{\int_X \text{id}_{[p,1]}(g_A) g_A \, dx}{\int_X dx}, \qquad (28)$$

where g_A is a stochastic basin of attraction, $\text{id}_{[p,1]}(g_A)$ is an indicator function, which is equal to 1 if $g_A \in [p,1]$ and zero otherwise, and p is the required probability threshold, between 0 and 1. This expression is a particular case of equation (44) in [78], with $\rho_{pert}(x)$ as a uniform density over the phase-space window X, and also reduces to the global integrity measure (GIM) [79] in the deterministic limit. Figure 16 shows the results for $0 \leq \sigma \leq 2$ and $1/\varepsilon = 10^9$. The nonresonant attractor dynamic integrity, Figure 16(a), corroborates its resilience to noisy perturbations, with its basin area being practically constant for $\sigma < 1.6$. Also, the probability is practically equal to one for all initial conditions. For $\sigma > 1.6$, the integrity measure increases, but the results show a more marked variation of the probability with large regions with $p < 0.5$. However, the basin area with probability $p = 1.0$ remains practically constant. The resonant attractor dynamic integrity measure, Figure 16(b), shows a steady decline, with an abrupt Dover cliff integrity loss at $\sigma = 1.6$, as already observed in Figure 12. If a conservative p-value is required, for example, $p \geq 0.8$, then the constant decline of the basin area can be viewed as a warning for $\sigma < 1.6$.

Continuing the discussion of the dynamic integrity, its dependency on the adopted time-horizon is illustrated in Figure 17, where the variation of the basin area is plotted for increasing values of the time-horizon $1/\varepsilon$ for selected probability thresholds p. Initially, the basin area increases up to a plateau, as expected for short transients, and between 10^2 and 10^6 periods of excitation the integrity of both attractors remains practically unchanged; however, the resonant attractor shows a significant dependence on the required probability threshold, indicating its high sensitivity to noise.

The basin area only changes after 10^6 periods of excitation, with the resonant basin vanishing completely after 10^9 periods. Classical methods, which rely on the time integration of each initial condition up to the time-horizon, would be too expensive to represent the permanent state of this system. Therefore, the approximation of the flow structure in phase-space becomes advantageous, considerably diminishing the computational cost.

The adopted hierarchical phase-space discretization reduced the total number of integrated initial conditions by at least 30%, in comparison with a uniform discretization of the phase-space, for all noise intensities. This again demonstrates the efficiency of the proposed methodology [46], when compared to a full phase-space discretization.

7.2 Effects of parametric uncertainty of the damping ratio

As shown in the previous sections, damping has a critical influence on the global dynamics of the microarch. However, damping is usually difficult to model or measure since it stems from different sources. Thus, it is important to investigate the influence of damping uncertainty on global dynamics. The variation of the frequency responses in Figure 6 to Figure 8 demonstrates how the superharmonic oscillations vary with the damping ratio ξ. However, as an estimated parameter, it is usually associated with a distribution, defined as a random parameter of a given probability space. To better understand how this uncertainty affects the global response, the effects of this assumption on the superharmonic global dynamics of the harmonically excited microarch for $A = 17V$ and $\Omega = 15$, is investigated. Here, a modified refinement algorithm, see [46], is applied in conjunction with a probability space discretization, explained in [46], to obtain mean global structures.

The damping ratio is assumed as uniformly distributed over the real continuous interval $[a, b]$, that is, $\xi \sim U(a, b)$. The computation of the mean structures is accomplished through the Gauss-Legendre quadrature, a common choice for treating uniform random variables through spectral expansion [80]. Taking ξ_{std} as a standard random variable uniformly distributed over [-1, 1], $\xi_{std} \sim U(-1, 1)$, the damping ratio can be defined as

$$\xi(\xi_{std}) = \frac{(b-a)}{2}\xi_{std} + \frac{(b+a)}{2}.$$ (29)

It is clear that $\xi(-1) = a$ and $\xi(1) = b$. The probability $P_\xi[\xi \le X]$ is given by

$$\int_a^{X(x)} \xi f(\xi)d\xi =$$
$$\frac{1}{2}\int_{-1}^{x}\left\{\frac{(b-a)}{2}\xi_{std} + \frac{(b+a)}{2}\right\}d\xi_{std},$$ (30)

where $f(\xi)$ is the probability density of ξ. Differentiating both sides of equation (30) with respect to x and applying equation (29) by taking $\xi = X$ and $\xi_{std} = x$, one obtains

$$f(\xi) = \begin{cases} \dfrac{1}{b-a} & \forall \xi \in [a,b], \\ 0 & \forall \xi \notin [a,b]. \end{cases}$$ (31)

Therefore, the damping ratio $\xi \sim U(a, b)$ can be represented by equation (29). This allows the Gauss-Legendre quadrature in [80] to be applied for ξ_{std}, and the original ξ is obtained through equation (29). In the following application, ten collocation points are adopted, discretizing the probability space into 10 points. Then, after obtaining the attractors' densities and basins observables for each ξ-value, see Appendix B, discretized mean structures are computed. For details, refer to [46].

Four cases are considered adopting $a = 0.04, 0.03, 0.02, 0.01$, and $b = 0.05$. The interval $[a, b] = [0.04, 0.05]$ represents a low uncertainty case, and the interval $[a, b] = [0.01, 0.05]$ represents a high uncertainty case. Figure 18 shows the mean basins' observables and attractors' distributions for the four cases, showing how these structures change as uncertainty increases. In the first case with $\xi \sim U(0.04,0.05)$, Figure 18(a), the effect of uncertainty is already evident in the mean basins, diffusing their boundaries. That is, regions with probabilities different from 0 and 1 to converge to either attractor start to appear. Again, these regions are referred to as nondeterministic. The uncertainty already affects the resonant attractor, with its mean distribution forming a curve in the phase-space. The nonresonant attractor, however, stays localized. This pattern is observed for all uncertainty cases, with the resonant attractor mean distribution spreading over a curve in phase-space as uncertainty increases. Also, the nonresonant mean basin diffusion depicts increasing regions with probability lower than one. In the last case, Figure 18(d), large nondeterministic regions are observed for both attractors, and the deterministic region of the resonant attractor is confined to a small area in phase-space. This suggests that the resonant attractor is sensitive to uncertainty in the damping ratio.

Figure 18(.3) shows how the escape region is affected by the uncertainty in the damping ratio. As the uncertainty increases, nondeterministic escape zones inside the original deterministic basins of attraction regions appear. The last case, Figure 18(d.3), demonstrates how large uncertainties deteriorate the classical basins of attraction, with large

nondeterministic regions. Finally, the results are time-independent since the parametric uncertainty of ξ does not depend on time. Therefore, there is no influence of the time-horizon on the stochastic basins. Classical global analysis methods, such as the Grid of starts, could be considered with low time-horizons, with the uncertainty addressed, for example, through a Monte-Carlo method. However, this would still be computationally expensive since such a method demands that initial conditions are integrated until the time-horizon is reached, whereas the Ulam method/Generalized cell-mapping approximates the phase-space flow through only one period of integration for each set of initial conditions. Additionally, the hierarchical phase-space discretization led to an economy of at least 60% in the total number of integrated initial conditions, for all uncertainty levels. This demonstrates once more the efficiency of the proposed methodology [46], when compared to a full phase-space discretization.

The process of basins' erosion and the complexity of their boundaries for increasing uncertainties, observed in Figure 18, is correlated to the uncertainty effects on the manifolds, see [46]. This correlation will be a topic of future investigations.

Figure 19 displays the dynamic integrity profiles computed through equation (28) for the analyzed uncertainty cases as functions of the lower parameter boundary a. The first case, $a = 0.05$, corresponds to the deterministic result with $\xi = 0.05$. The nonresonant attractor shows a steady integrity decrease for all probability thresholds p. Surprisingly, the resonant basin shows two distinct patterns: for a probability threshold $p < 0.8$ the integrity increases before decreasing, and for $p > 0.8$ the integrity always decreases. Therefore, the system can gain or lose integrity for mild uncertainty cases, depending on the adopted probability threshold p.

8. Conclusions

Uncertainties in microelectromechanical systems are unavoidable and can drastically change their behavior. Also, noise is inevitable in the operational stages. The computational cost of both global dynamic and nondeterministic analysis makes it difficult to consider these phenomena simultaneously in such a complex system. Here, a recent adaptative phase-space discretization strategy [46] was applied to a microarch electrically actuated. Clamped-clamped boundary conditions, an initial stress-free curvature, and imposed axial displacement were considered. The axial displacement was condensed, and a flexural beam model was derived. Its static response under DC actuation displayed two limit points which delimit the unstable solutions branch and lead to a multistability range and hysteresis. It was shown that two symmetric linear modes are the minimum necessary for qualitative analysis.

A reduced order model, based on the first two symmetric linear modes, was derived for the dynamics in the vicinity of a given static position, following the definition of nonlinear

normal modes of Shaw and Pierre [72]. The free vibration response and the frequency response under AC actuation demonstrated the validity of the proposed model when compared against the classical 2-mode discretization. A main superharmonic resonant region was identified, with the primary resonant region being excited only for low damping ratios. In all cases, a softening response was obtained due to the initial beam curvature and load.

The adaptative phase-space discretization of stable and unstable manifolds with an r-tree data structure presented in [46] was employed. The global dynamics in the superharmonic region was studied. A potential well with nonresonant and resonant solutions was observed, and the impact of different damping ratios and added noise was investigated. The basins of the deterministic case demonstrated a convoluted partition of the phase-space for low damping ratios. Then, a low damping ratio case was investigated under noise, and the transient characteristic of solutions under high noise levels was observed, similar to previous results in [35]. This was evidenced in the integrity profiles, which display a Dover cliff pattern when the noise amplitude varies, along with a dependency on the adopted time-horizon (integration time). Finally, the influence of the uncertainty of the critical damping ratio was investigated, with a uniform distribution being adopted. The spread of the attractors along the bifurcation path as the distribution interval increases was observed, a distinct result in comparison to noisy cases. Their basins also spread over the phase-space. The integrity profiles revealed the gradual integrity loss of both solutions.

The adaptative discretization strategy adopted proved to be efficient when compared to a full phase-space discretization, in the context of a MEMS device. Additionally, the important role of nondeterministic global dynamics in unveiling the nonlinear response and actual safety of microengineering systems was highlighted.

Declaration of Competing Interest

The authors declare that they have no known competing financial interests or personal relationships that could have appeared to influence the work reported in this paper.

Acknowledgments

Data availability

The raw data required to reproduce these findings are available on request. The processed data required to reproduce these findings are available on request.

References

[1] Senturia S D 2002 *Microsystem Design* (New York, NY: Springer New York)

[2] Younis M I 2011 *MEMS Linear and Nonlinear Statics and Dynamics* vol 20 (New York, NY: Springer New York)

[3] Brand O, Dufour I, Heinrich S M and Josse F 2015 *Resonant MEMS: Fundamentals, Implementation, and Application* (Wiley-VCH Verlag GmbH & Co. KGaA)

[4] Lyshevski S E 2018 *MEMS and NEMS: Systems, Devices, and Structures* (CRC Press)

[5] Di Barba P and Wiak S 2020 *MEMS: Field Models and Optimal Design* vol 573 (Cham: Springer International Publishing)

[6] Lenci S and Rega G 2006 Control of pull-in dynamics in a nonlinear thermoelastic electrically actuated microbeam *J. Micromechanics Microengineering* **16** 390–401

[7] Zhang W-M, Yan H, Peng Z-K and Meng G 2014 Electrostatic pull-in instability in MEMS/NEMS: A review *Sensors Actuators A Phys.* **214** 187–218

[8] Hajjaj A Z, Jaber N, Ilyas S, Alfosail F K and Younis M I 2020 Linear and nonlinear dynamics of micro and nano-resonators: Review of recent advances *Int. J. Non. Linear. Mech.* **119** 103328

[9] Khan F and Younis M I 2022 RF MEMS electrostatically actuated tunable capacitors and their applications: A review *J. Micromechanics Microengineering* **32** 013002

[10] Khaniki H B, Ghayesh M H and Amabili M 2021 A review on the statics and dynamics of electrically actuated nano and micro structures *Int. J. Non. Linear. Mech.* **129** 103658

[11] Verma G, Mondal K and Gupta A 2021 Si-based MEMS resonant sensor: A review from microfabrication perspective *Microelectronics J.* **118** 105210

[12] Corigliano A, Ghisi A, Mariani S and Zega V 2022 Mechanics of Microsystems: A Recent Journey in a Fascinating Branch of Mechanics *50+ Years of AIMETA* (Cham: Springer International Publishing) pp 419–35

[13] Hajjaj A Z, Jaber N, Hafiz M A A, Ilyas S and Younis M I 2018 Multiple internal resonances in MEMS arch resonators *Phys. Lett. Sect. A Gen. At. Solid State Phys.* **382** 3393–8

[14] Hu N and Burgueño R 2015 Buckling-induced smart applications: recent advances and trends *Smart Mater. Struct.* **24** 063001

[15] Fonseca F M and Gonçalves P B 2022 Nonlinear behavior and instabilities of a hyperelastic von Mises truss *Int. J. Non. Linear. Mech.* **142** 103964

[16] Hussein H, Khan F and Younis M I 2020 A monolithic tunable symmetric bistable mechanism *Smart Mater. Struct.* **29** 075033

[17] Ruzziconi L, Lenci S and Younis M I 2013 An imperfect microbeam under an axial load and electric excitation: Nonlinear phenomena and dynamical integrity *Int. J. Bifurc. Chaos* **23** 1350026

[18] Ruzziconi L, Lenci S and Younis M I 2019 Interpreting and Predicting Experimental Responses of Micro- and Nano-Devices via Dynamical Integrity *Global Nonlinear Dynamics for Engineering Design and System Safety* pp 113–66

[19] Ruzziconi L, Younis M I and Lenci S 2013 Multistability in an electrically actuated carbon nanotube: A dynamical integrity perspective *Nonlinear Dyn.* **74** 533–49

[20] Ruzziconi L, Younis M I and Lenci S 2013 An electrically actuated imperfect microbeam: Dynamical integrity for interpreting and predicting the device response *Meccanica* **48** 1761–75

[21] Settimi V and Rega G 2016 Exploiting global dynamics of a noncontact atomic force microcantilever to enhance its dynamical robustness via numerical control *Int. J. Bifurc. Chaos* **26** 1630018

[22] Rega G, Lenci S and Ruzziconi L 2019 Dynamical Integrity: A Novel Paradigm for Evaluating Load Carrying Capacity *Global Nonlinear Dynamics for Engineering Design and System Safety* pp 27–112

[23] Rega G and Settimi V 2021 Global dynamics perspective on macro- to nano-mechanics *Nonlinear Dyn.* **103** 1259–303

[24] Rega G 2022 Nonlinear dynamics in mechanics: state of the art and expected future developments *J. Comput. Nonlinear Dyn.* **17**

[25] Vig J R and Kim Y 1999 Noise in microelectromechanical system resonators *IEEE Trans. Ultrason. Ferroelectr. Freq. Control* **46** 1558–65

[26] Andò B, Baglio S, Trigona C, Dumas N, Latorre L and Nouet P 2010 Nonlinear mechanism in MEMS devices for energy harvesting applications *J. Micromechanics Microengineering* **20** 125020

[27] Alsaleem F M, Younis M I and Ouakad H M 2009 On the nonlinear resonances and dynamic pull-in of electrostatically actuated resonators *J. Micromechanics Microengineering* **19** 045013

[28] Ruzziconi L, Bataineh A M, Younis M I, Cui W and Lenci S 2013 Nonlinear dynamics of an electrically actuated imperfect microbeam resonator: experimental investigation and reduced-order modeling *J. Micromechanics Microengineering* **23** 075012

[29] Hajjaj A Z, Alfosail F K, Jaber N, Ilyas S and Younis M I 2020 Theoretical and experimental investigations of the crossover phenomenon in micromachined arch resonator: part I—linear problem *Nonlinear Dyn.* **99** 393–405

[30] Farokhi H and Ghayesh M H 2016 Size-dependent parametric dynamics of imperfect microbeams *Int. J. Eng. Sci.* **99** 39–55

[31] Farokhi H, Ghayesh M H and Amabili M 2013 Nonlinear dynamics of a geometrically imperfect microbeam based on the modified couple stress theory *Int. J. Eng. Sci.* **68** 11–23

[32] Dai H L and Wang L 2017 Size-dependent pull-in voltage and nonlinear dynamics of electrically actuated microcantilever-based MEMS: A full nonlinear analysis *Commun. Nonlinear Sci. Numer. Simul.* **46** 116–25

[33] Kamiński M and Corigliano A 2015 Numerical solution of the Duffing equation with random coefficients *Meccanica* **50** 1841–53

[34] Agarwal N and Aluru N R 2009 Stochastic Analysis of Electrostatic MEMS Subjected to Parameter Variations *J. Microelectromechanical Syst.* **18** 1454–68

[35] Benedetti K C B and Gonçalves P B 2022 Nonlinear response of an imperfect microcantilever static and dynamically actuated considering uncertainties and noise *Nonlinear Dyn.* **107** 1725–54

[36] Ulam S M 1964 *Problems in Modern Mathematics* (New York, NY: John Wiley & Sons)

[37]   Hsu C S 1981 A generalized theory of cell-to-cell mapping for nonlinear dynamical systems *J. Appl. Mech.* **48** 634–42

[38]   Hsu C S 1980 A theory of cell-to-cell mapping dynamical systems *J. Appl. Mech.* **47** 931–9

[39]   Guder R and Kreuzer E J 1997 Using generalized cell mapping to approximate invariant measures on compact manifolds *Int. J. Bifurc. Chaos* **07** 2487–99

[40]   Andonovski N and Lenci S 2019 Six-dimensional basins of attraction computation on small clusters with semi-parallelized SCM method *Int. J. Dyn. Control* 1–12

[41]   Belardinelli P and Lenci S 2016 A first parallel programming approach in basins of attraction computation *Int. J. Non. Linear. Mech.* **80** 76–81

[42]   Belardinelli P and Lenci S 2016 An efficient parallel implementation of cell mapping methods for MDOF systems *Nonlinear Dyn.* **86** 2279–90

[43]   Orlando D, Gonçalves P B, Rega G and Lenci S 2019 Influence of transient escape and added load noise on the dynamic integrity of multistable systems *Int. J. Non. Linear. Mech.* **109** 140–54

[44]   Silva F M A da and Gonçalves P B 2015 The influence of uncertainties and random noise on the dynamic integrity analysis of a system liable to unstable buckling *Nonlinear Dyn.* **81** 707–24

[45]   Benedetti K C B, Gonçalves P B, Lenci S and Rega G 2022 An operator methodology for the global dynamic analysis of stochastic nonlinear systems *Theor. Appl. Mech. Lett.* 100419

[46]   Benedetti K C B 2022 *Global Analysis of Stochastic Nonlinear Dynamical Systems: an Adaptive Phase-Space Discretization Strategy* (Pontifical Catholic University of Rio de Janeiro)

[47]   Younis M I, Abdel-Rahman E M and Nayfeh A H 2003 A reduced-order model for electrically actuated microbeam-based MEMS *J. Microelectromechanical Syst.* **12** 672–80

[48]   Hajjaj A Z, Alfosail F K, Jaber N, Ilyas S and Younis M I 2020 Theoretical and experimental investigations of the crossover phenomenon in micromachined arch resonator: part II—simultaneous 1:1 and 2:1 internal resonances *Nonlinear Dyn.* **99** 407–32

[49]   Ruzziconi L, Bataineh A M, Younis M I and Lenci S 2012 An Imperfect Microbeam Electrically Actuated: Experimental Investigation and Parameter Identification *ASME 2012 International Design Engineering Technical Conferences and Computers and Information in Engineering Conference* vol 5 (American Society of Mechanical Engineers) pp 87–94

[50]   Ruzziconi L, Younis M I and Lenci S 2013 Parameter identification of an electrically actuated imperfect microbeam *Int. J. Non. Linear. Mech.* **57** 208–19

[51]   Alkharabsheh S A and Younis M I 2013 Dynamics of MEMS arches of flexible supports *J. Microelectromechanical Syst.* **22** 216–24

[52]   Ghayesh M H 2018 Functionally graded microbeams: Simultaneous presence of imperfection and viscoelasticity *Int. J. Mech. Sci.* **140** 339–50

[53]   Caruntu D I, Martinez I and Knecht M W 2016 Parametric resonance voltage response of electrostatically actuated Micro-Electro-Mechanical Systems cantilever resonators *J. Sound Vib.* **362** 203–13

[54]   Caruntu D I, Botello M A, Reyes C A and Beatriz J S 2019 Voltage–Amplitude response of superharmonic resonance of second order of electrostatically actuated MEMS cantilever resonators *J. Comput. Nonlinear Dyn.* **14** 1–8

[55]   Hu Y C, Chang C M and Huang S C 2004 Some design considerations on the electrostatically actuated microstructures *Sensors Actuators A Phys.* **112** 155–61

[56]   Batra R C, Porfiri M and Spinello D 2006 Electromechanical model of electrically actuated narrow microbeams *J. Microelectromechanical Syst.* **15** 1175–89

[57]   Das K and Batra R C 2009 Pull-in and snap-through instabilities in transient deformations of microelectromechanical systems *J. Micromechanics Microengineering* **19** 035008

[58]   Das K and Batra R C 2009 Symmetry breaking, snap-through and pull-in instabilities under dynamic loading of microelectromechanical shallow arches *Smart Mater. Struct.* **18** 115008

[59]   Awrejcewicz J, Krysko V A, Pavlov S P, Zhigalov M V., Kalutsky L A and Krysko A V. 2019 Thermoelastic vibrations of a Timoshenko microbeam based on the modified couple stress theory *Nonlinear Dyn.*

[60]   Akhavan H, Roody B S, Ribeiro P and Fotuhi A R 2019 Modes of vibration, stability and internal resonances on non-linear piezoelectric small-scale beams *Commun. Nonlinear Sci. Numer. Simul.* **72** 88–107

[61]   Dai H L, Wang L and Ni Q 2014 Dynamics and pull-in instability of electrostatically actuated microbeams conveying fluid *Microfluid. Nanofluidics* **18** 49–55

[62]   Dehrouyeh-Semnani A M, Mostafaei H and Nikkhah-Bahrami M 2016 Free flexural vibration of geometrically imperfect functionally graded microbeams *Int. J. Eng. Sci.* **105** 56–79

[63]   Ghayesh M H, Farokhi H and Amabili M 2013 Nonlinear dynamics of a microscale beam based on the modified couple stress theory *Compos. Part B Eng.* **5035** 318–24

[64]   Touzé C, Vizzaccaro A and Thomas O 2021 Model order reduction methods for geometrically nonlinear structures: a review of nonlinear techniques *Nonlinear Dyn.* **105** 1141–90

[65]   Mazzilli C E N, Gonçalves P B and Franzini G R 2022 Reduced-order modelling based on non-linear modes *Int. J. Mech. Sci.* **214** 106915

[66]   Ruzziconi L, Lenci S, Cocchi G and Younis M I 2014 A MEMS device electrically actuated: Global dynamics and dynamical integrity *EURODYN 2014 Proceedings of the 9th International Conference on Structural Dynamics* (Porto) pp 2005–12

[67]   Nayfeh A H and Pai P F 2004 *Linear and Nonlinear Structural Mechanics* (Wiley)

[68]   Han S M, Benaroya H and Wei T 1999 Dynamics of transversely vibrating beams using four engineering theories *J. Sound Vib.* **225** 935–88

[69]   BIPM 2019 *The international system of units (SI)* (Bureau International des Poids et Mesures)

[70]   Nayfeh A H and Mook D T 1995 *Nonlinear Oscillations* (Wiley)

[71]   Moon F C 2004 *Chaotic Vibrations* (Wiley)

[72]   Shaw S W and Pierre C 1993 Normal modes for non-linear vibratory systems *J. Sound Vib.* **164** 85–124

[73]   Mazzilli C E N and Baracho Neto O G P 2002 Evaluation of non-linear normal modes for finite-element models *Comput. Struct.* **80** 957–65

[74]   Dankowicz H and Schilder F 2013 *Recipes for Continuation* (Philadelphia, PA: Society for Industrial and Applied Mathematics)

[75]   Ouakad H M and Younis M I 2014 On using the dynamic snap-through motion of MEMS initially curved microbeams for filtering applications *J. Sound Vib.* **333** 555–68

[76]   Younis M I, Ouakad H M, Alsaleem F M, Miles R and Cui W 2010 Nonlinear Dynamics of MEMS Arches Under Harmonic Electrostatic Actuation *J. Microelectromechanical Syst.* **19** 647–56

[77]   Najar F, Nayfeh A H, Abdel-Rahman E M, Choura S and El-Borgi S 2010 Nonlinear analysis of MEMS electrostatic microactuators: Primary and secondary resonances of the first mode *J. Vib. Control* **16** 1321–49

[78]   Lindner M and Hellmann F 2019 Stochastic basins of attraction and generalized committor functions *Phys. Rev. E* **100** 022124

[79]   Benedetti K C B, Gonçalves P B and Silva F M A da 2020 Nonlinear oscillations and bifurcations of a multistable truss and dynamic integrity assessment via a Monte Carlo approach *Meccanica* **55** 2623–57

[80]   Le Maître O P and Knio O M 2010 *Spectral Methods for Uncertainty Quantification* (Dordrecht: Springer Netherlands)

[81]   Hsu C S 1987 *Cell-to-Cell Mapping* vol 64 (New York, NY: Springer New York)

[82]   Sun J-Q and Hsu C S 1990 The generalized cell mapping method in nonlinear random vibration based upon short-time gaussian approximation *J. Appl. Mech.* **57** 1018–25

[83]   Nayfeh A H and Balachandran B 1995 *Applied Nonlinear Dynamics* (New York: Wiley)

Appendix A: Constant tensors resulting from the Galerkin expansion of the microarch problem

$$\mathbf{A}_{in} = \int_0^1 (1-w_0)^2 F_i F_n \, ds, \tag{A1}$$

$$\mathbf{A}_{ijn} = \int_0^1 2(1-w_0) F_i F_j F_n \, ds, \tag{A2}$$

$$\mathbf{A}_{ijkn} = \int_0^1 F_i F_j F_k F_n \, ds, \tag{A3}$$

$$\mathbf{B}_{in} = \int_0^1 (1-w_0)^2 F_i^{\text{iv}} F_n \, ds, \tag{A4}$$

$$\mathbf{B}_{ijn} = \int_0^1 2(1-w_0) F_i^{\text{iv}} F_j F_n \, ds, \tag{A5}$$

$$\mathbf{B}_{ijkn} = \int_0^1 F_i^{\text{iv}} F_j F_k F_n \, ds, \tag{A6}$$

$$\mathbf{C}_n = u_B \int_0^1 (1-w_0)^2 w_0'' F_n \, ds, \tag{A7}$$

$$\mathbf{C}_{in} = -\int_0^1 d^2 w_0' F_i' \, ds \int_0^1 (1-w_0)^2 w_0'' F_n \, ds$$
$$+ u_B \left(\int_0^1 (1-w_0)^2 F_i'' F_n \, ds \right. \tag{A8}$$
$$\left. - \int_0^1 2(1-w_0) w_0'' F_i F_n \, ds \right),$$

$$\mathbf{C}_{ijn} = -u_B \left(\int_0^1 2(1-w_0) F_i'' F_j F_n \, ds - \int_0^1 w_0'' F_i F_j F_n \, ds \right)$$
$$- \int_0^1 \frac{d^2}{2} F_i' F_j' \, ds \int_0^1 (1-w_0)^2 w_0'' F_n \, ds$$
$$- \int_0^1 d^2 w_0' F_j' \, ds \left(\int_0^1 (1-w_0)^2 F_i'' F_n \, ds \right. \tag{A9}$$
$$\left. - \int_0^1 2(1-w_0) w_0'' F_i F_n \, ds \right),$$

$$\mathbf{C}_{ijkn} = u_B \int_0^1 F_i'' F_j F_k F_n \, ds$$
$$+ \int_0^1 d^2 w_0' F_k' \, ds \left(\int_0^1 w_0'' F_i F_j F_n \, ds \right.$$
$$\left. - \int_0^1 2(1-w_0) F_i'' F_j F_n \, ds \right) \tag{A10}$$
$$- \int_0^1 \frac{d^2}{2} F_k' F_j' \, ds \left(\int_0^1 (1-w_0)^2 F_i'' F_n \, ds \right.$$
$$\left. - \int_0^1 2(1-w_0) w_0'' F_i F_n \, ds \right),$$

$$\mathbf{C}_{ijkln} = -\int_0^1 d^2 w_0' F_l' \, ds \int_0^1 F_i'' F_j F_k F_n \, ds$$
$$+ \int_0^1 \frac{d^2}{2} F_k' F_l' \, ds \left(\int_0^1 2(1-w_0) F_i'' F_j F_n \, ds \right. \tag{A11}$$
$$\left. - \int_0^1 w_0'' F_i F_j F_n \, ds \right)$$

$$\mathbf{C}_{ijklmn} = -\int_0^1 \frac{d^2}{2} F_l' F_m' \, ds \int_0^1 F_i'' F_j F_k F_n \, ds, \tag{A12}$$

$$\mathbf{D}_n = u_B \int_0^1 (1-w_0)^2 w_0^{\text{iv}} F_n \, ds$$
$$+ u_B \int_0^1 (1-w_0)^2 d^2 \left\{ w_0' \left(F_i'' w_0' \right)' \right\}' F_n \, ds, \tag{A13}$$

$$\mathbf{D}_{in} = \int_0^1 w_0' F_i''' \, ds \int_0^1 (1-w_0)^2 \left(w_0'' + 2\frac{d^2}{\beta_u} w_0^{\text{iv}} \right) F_n \, ds$$
$$+ u_B \left(\int_0^1 2(1-w_0)^2 \left(F_i^{\text{iv}} - w_0^{\text{iv}} F_i \right) F_n \, ds \right)$$
$$+ \int_0^1 \frac{d^2}{\beta_u} (1-w_0)^2 \left(w_0'^2 F_i''' \right)'' F_n \, ds$$
$$+ \int_0^1 d^2 w_0' F_i' \, ds \int_0^1 (1-w_0)^2 w_0^{\text{iv}} F_n \, ds \tag{A14}$$
$$- \int_0^1 \frac{d^2}{\beta_u} (1-w_0)^2 w_0' F_j''' F_i''' F_n \, ds$$
$$+ \int_0^1 (1-w_0)^2 d^2 F_n \left(F_i'' w_0'' w_0' + F_i' w_0''^2 \right.$$
$$\left. + F_i' \left(w_0' w_0'' \right)' \right)' \, ds,$$

Benedetti *et al*

$$\mathbf{D}_{ijn} = \int_0^1 F_i'F_j'''ds \int_0^1 (1-w_0)^2 \left(w_0'' + 2\frac{d^2}{\beta_u} w_0^{\text{iv}} \right) F_n\,ds$$

$$+ u_B \left(\int_0^1 \left(4(1-w_0)F_i^{\text{iv}} - w_0^{\text{iv}} F_i \right) F_j F_n\,ds \right)$$

$$+ \int_0^1 w_0' F_j'''ds \left(\int_0^1 (1-w_0)^2 \left(F_i'' + 2\frac{d^2}{\beta_u} F_i^{\text{iv}} \right) F_n\,ds \right.$$

$$\left. - \int_0^1 2(1-w_0)\left(w_0'' + 2\frac{d^2}{\beta_u} w_0^{\text{iv}} \right) F_i F_n\,ds \right)$$

$$+ \int_0^1 \frac{d^2}{2} F_i'F_j'ds \int_0^1 (1-w_0)^2 w_0^{\text{iv}} F_n\,ds$$

$$+ \int_0^1 d^2 w_0' F_i'ds \left(\int_0^1 2(1-w_0)^2 F_i^{\text{iv}} F_n\,ds \right.$$

$$\left. - \int_0^1 2(1-w_0) w_0^{\text{iv}} F_j F_n\,ds \right) \qquad (A15)$$

$$- \int_0^1 2d^2(1-w_0) F_j \left(F_i' w_0''^2 + F_i'(w_0' w_0'')' \right)' F_n\,ds$$

$$+ \int_0^1 \left\{ d^2(1-w_0)^2 \left(F_i''F_j'w_0'' + F_j'(F_i''w_0')' \right. \right.$$

$$\left. \left. + w_0'\left(F_i''F_j' \right)' - \frac{F_i'F_j'w_0'''}{2} \right)' F_n \right\} ds$$

$$+ \int_0^1 2\frac{d^2}{\beta_u}(1-w_0)^2 \left(w_0'F_j'F_i''' \right)'' F_n\,ds$$

$$+ \int_0^1 2\frac{d^2}{\beta_u}(1-w_0) F_j \left(w_0'^2 F_i''' \right)'' F_n\,ds$$

$$- \int_0^1 2d^2(1-w_0) F_j \left(F_i''w_0''w_0' + w_0'(F_i''w_0')' \right)' F_n\,ds,$$

$$\mathbf{D}_{ijkn} = \int_0^1 F_j'F_k'''ds \int_0^1 (1-w_0)^2 \left(F_i'' + 2\frac{d^2}{\beta_u} F_i^{\text{iv}} \right) F_n\,ds$$

$$- \int_0^1 F_j'F_k'''ds \int_0^1 2(1-w_0)\left(w_0'' + 2\frac{d^2}{\beta_u} w_0^{\text{iv}} \right) F_i F_n\,ds$$

$$+ \int_0^1 w_0'F_k'''ds \int_0^1 \left(w_0'' + 2\frac{d^2}{\beta_u} w_0^{\text{iv}} \right) F_i F_j F_n\,ds$$

$$- \int_0^1 w_0'F_k'''ds \int_0^1 2(1-w_0)\left(F_i'' + 2\frac{d^2}{\beta_u} F_i^{\text{iv}} \right) F_j F_n\,ds$$

$$- u_B \int_0^1 2F_i^{\text{iv}} F_j F_k F_n\,ds$$

$$+ \int_0^1 \frac{d^2}{2} F_j'F_k'ds \left(\int_0^1 2(1-w_0)w_0^{\text{iv}} F_i F_n\,ds \right.$$

$$\left. - \int_0^1 2(1-w_0)^2 F_i^{\text{iv}} F_n\,ds \right)$$

$$- \int_0^1 d^2 w_0'F_k'ds \left(\int_0^1 4(1-w_0) F_i^{\text{iv}} F_j F_n\,ds \right.$$

$$\left. - \int_0^1 w_0^{\text{iv}} F_i F_j F_n\,ds \right)$$

$$+ \int_0^1 d^2(1-w_0) F_k \left(F_i'F_j'w_0''' \right)' F_n\,ds$$

$$+ \int_0^1 d^2 F_j F_k \left(F_i'w_0''^2 + F_i'(w_0'w_0'')' \right)' F_n\,ds \qquad (A16)$$

$$+ \int_0^1 d^2(1-w_0)^2 \left(F_j'(F_i''F_k')' \right)' F_n\,ds$$

$$- \int_0^1 2d^2(1-w_0) F_k F_n \left(F_i''F_j'w_0'' + F_j'(F_i''w_0')' \right.$$

$$\left. + w_0'\left(F_i''F_j' \right)' \right)' ds$$

$$+ \int_0^1 d^2 F_j F_k \left(F_i''w_0''w_0' + w_0'(F_i''w_0')' \right)' F_n\,ds$$

$$+ \int_0^1 \frac{d^2}{\beta_u}(1-w_0)^2 \left(F_j'F_k'F_i''' \right)'' F_n\,ds$$

$$+ \int_0^1 4\frac{d^2}{\beta_u}(1-w_0) F_k \left(w_0'F_j'F_i''' \right)'' F_n\,ds$$

$$+ \int_0^1 \frac{d^2}{\beta_u} F_j F_k \left(w_0'^2 F_i''' \right)'' F_n\,ds$$

$$- \int_0^1 \frac{d^2}{\beta_u}(1-w_0)^2 F_k'F_j'''F_i'''F_n\,ds$$

$$+ \int_0^1 2\frac{d^2}{\beta_u}(1-w_0) F_k w_0'F_j'''F_i'''F_n\,ds,$$

J. Micromech. Microeng. **XX** (XXXX) XXXXXX

Benedetti *et al*

$$\mathbf{D}_{ijkln} = \int_0^1 F_k'F_l'''ds \int_0^1 \left(w_0'' + 2\frac{d^2}{\beta_u} w_0^{\text{iv}} \right) F_i F_j F_n \, ds$$

$$- \int_0^1 F_k'F_l'''ds \int_0^1 2(1-w_0)\left(F_i'' + 2\frac{d^2}{\beta_u} F_i^{\text{iv}} \right) F_j F_n \, ds$$

$$+ \int_0^1 w_0'F_l'''ds \int_0^1 \left(F_i'' + 2\frac{d^2}{\beta_u} F_i^{\text{iv}} \right) F_j F_k F_n \, ds$$

$$+ \int_0^1 d^2 w_0' F_i' ds \int_0^1 2F_i^{\text{iv}} F_j F_k F_n \, ds$$

$$+ \int_0^1 \frac{d^2}{2} F_k'F_l'ds \left(\int_0^1 w_0^{\text{iv}} F_i F_j F_n \, ds \right.$$

$$- \int_0^1 4(1-w_0)F_i^{\text{iv}} F_j F_n \, ds \right)$$

$$- \int_0^1 F_k F_l \frac{d^2}{2} \left(F_i'F_j'w_0''' \right)' F_n \, ds$$

$$- \int_0^1 2(1-w_0)F_l d^2 \left(F_j'\left(F_i''F_k' \right)' \right)' F_n \, ds \qquad \text{(A17)}$$

$$+ \int_0^1 d^2 F_k F_l F_n \left(F_i''F_j'w_0'' + F_j'\left(F_i''w_0' \right)' \right.$$

$$+ w_0'\left(F_i''F_j' \right)' \right)' ds$$

$$+ \int_0^1 2\frac{d^2}{\beta_u}(1-w_0)F_l \left(F_j'F_k'F_i''' \right)'' F_n \, ds$$

$$+ \int_0^1 2\frac{d^2}{\beta_u} F_k F_l \left(w_0'F_j'F_i''' \right)'' F_n \, ds$$

$$+ \int_0^1 2\frac{d^2}{\beta_u}(1-w_0)F_l F_k'F_j'''F_i''' F_n \, ds$$

$$- \int_0^1 \frac{d^2}{\beta_u} w_0'F_k F_l F_j'''F_i''' F_n \, ds,$$

$$\mathbf{D}_{ijklmn} = \int_0^1 \left(F_i'' + 2\frac{d^2}{\beta_u} F_i^{\text{iv}} \right) F_j F_k F_n \, ds \int_0^1 F_l'F_m''' ds$$

$$+ \int_0^1 2F_i^{\text{iv}} F_j F_k F_n \, ds \int_0^1 \frac{d^2}{2} F_l'F_m' ds$$

$$+ \int_0^1 d^2 F_l F_m \left(F_j'\left(F_i''F_k' \right)' \right)' F_n \, ds \qquad \text{(A18)}$$

$$+ \int_0^1 \frac{d^2}{\beta_u} F_l F_m \left(F_j'F_k'F_i''' \right)'' F_n \, ds$$

$$- \int_0^1 \frac{d^2}{\beta_u} F_l F_m F_k'F_j'''F_i''' F_n \, ds.$$

Appendix B: Discretized transfer operator approach for nondeterministic dynamics

In the framework of an operator approach for the analysis of global dynamics, a concise description of the construction of the discretized operators is summarized here, along with the information given by them. Detailed expositions can be found in [45,46].

Initially, a phase-space window of interest X is partitioned into a finite collection of n disjoint boxes $\mathbf{B} = \{b_1, \ldots., b_n\}$. Such a collection is also referred to as cell space in the cell-mapping literature [38,40–42,81,82]. Then, initial conditions in each box are integrated for a period of time T (the same period that defines the stroboscopic Poincaré map [83]). Assumed a set of initial conditions within a given box b_i, the transfer probability between boxes is approximated by

$$p_{ij} = \frac{\#\text{states in } b_j \text{ after } 1T}{\#\text{i.c. in } b_i}. \qquad \text{(B1)}$$

The matrix p_{ij} approximates the continuous Perron-Frobenius operator $\mathbf{P}_t$ for a time-interval $1T$. Given a phase-space subdivision into n boxes, p_{ij} is a $n \times n$ row stochastic matrix. Stochastic dynamical systems due to the presence of noise are considered by integrating the initial conditions repeatedly, and entries p_{ij} are computed through a Monte Carlo approach. The resulting transfer matrix approximates the continuous Foias operator $\mathbf{F}_t$ for the time-interval $1T$. For parametric uncertainty cases, given a parameter set of possible values λ, it is assumed that the transfer operators are functions of such set, resulting in the matrix $p_{ij}(\lambda)$ and approximating $\mathbf{P}_t(\lambda)$.

The left-fixed space of p_{ij}, that is, the solutions of

$$f_i(\lambda) p_{ij}(\lambda) = f_i(\lambda)\delta_{ij}, \qquad \text{(B2)}$$

where the vector $f_i(\lambda)$ contains information on attractors' distributions if the phase-space is sufficiently refined, holds for deterministic and stochastic dynamics, and a particular uncertainty parameter value λ. Once all attractors' distributions are computed, the basins are obtained following the definition of stochastic basins of attraction by Lindner and Hellmann [78]. Such basins are described by functions $g_{A(\lambda)}(x; \varepsilon)$ over the entire phase-space, giving the probability of a set of initial condition x to have converged to an attractor A until a time-horizon $1/\varepsilon$ is reached. This function, also named observable, is the solution of a linear ill-conditioned system, which is given in vector (discretized) form by

$$\left[\delta_{ij} - (1-\varepsilon) p_{ij} \right] g_j(\varepsilon; \lambda) = \varepsilon \, \text{id}_{A(\lambda)}. \qquad \text{(B3)}$$

The term $g_j(\varepsilon;\lambda)$ is the vector form of $g_{A(\lambda)}(x;\varepsilon)$ due to the phase-space discretization, while $\mathrm{id}_{A(\lambda)}$ is the phase-space indicator function of the attractor $A(\lambda)$ with discretized distribution $f_i(\lambda)$. In summary, $f_i(\lambda)$ and $g_j(\varepsilon;\lambda)$ are discretizations of the attractors' distributions and basins' observables, respectively, for deterministic or stochastic dynamics given a particular value of λ. In the case of uncertainty parameter, mean attractors and basins can be obtained from a discretization of the parameter space.

Benedetti *et al*
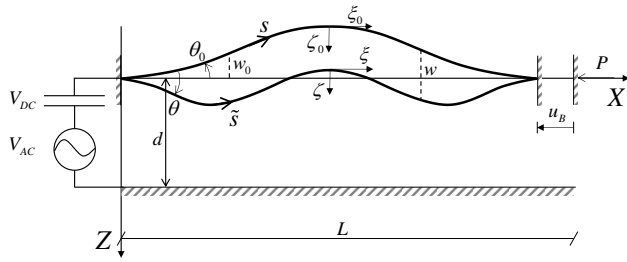
Figure 1. Orientation of imperfect undeformed and deformed coordinate
systems of the microarch with respect to the reference system
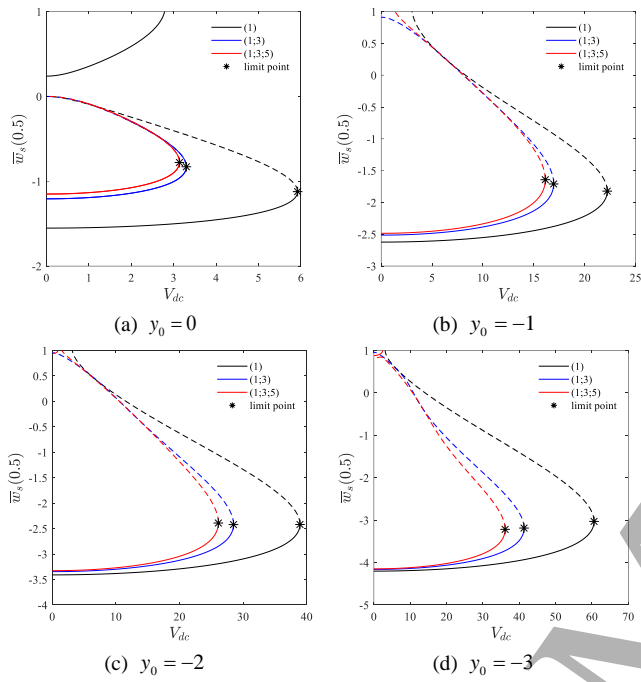
Figure 2. Comparison of the microarch static response for different modal
expansions and levels of initial imperfection. – stable, -- unstable

Benedetti *et al*
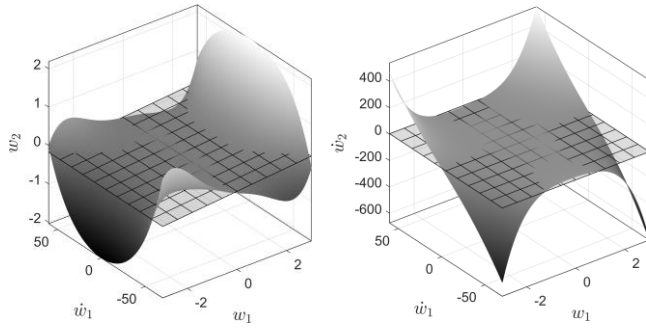
Figure 3. Two-dimensional invariant manifold of the reduced order model
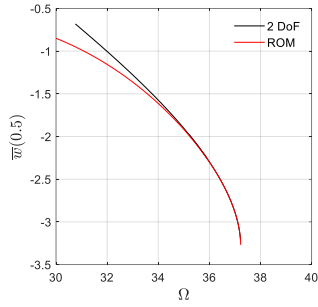
Figure 4. Backbone curves for the first mode natural frequency of the total displacement $\overline{w}$ at $s = 0.5$

(a) $\xi = 0.05$

(b) $\xi = 0.03$
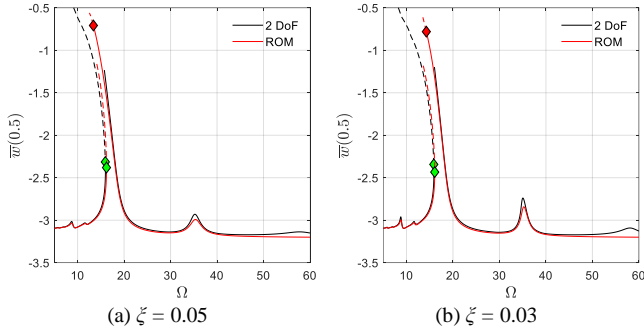
Figure 5. Resonance response curves for $A = 17$V and varying ξ. Saddle-nodes in green, period-doubling points in red. – stable, -- unstable
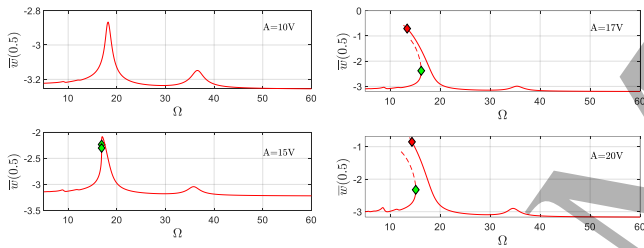
Figure 6. Resonance response curves of the reduced order model for $\xi = 0.05$ and varying amplitude A. Saddle-nodes in green, period-doubling points in red. – stable, -- unstable
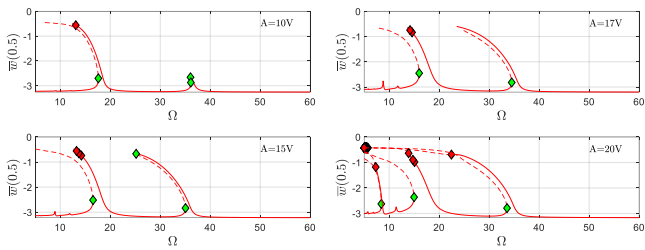
Benedetti *et al*
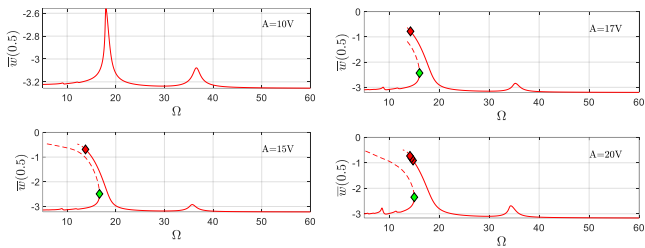
Figure 7. Resonance response curves of the reduced order model for $\xi = 0.03$ and varying amplitude *A*. Saddle-nodes in green, period-doubling points in red. – stable, -- unstable
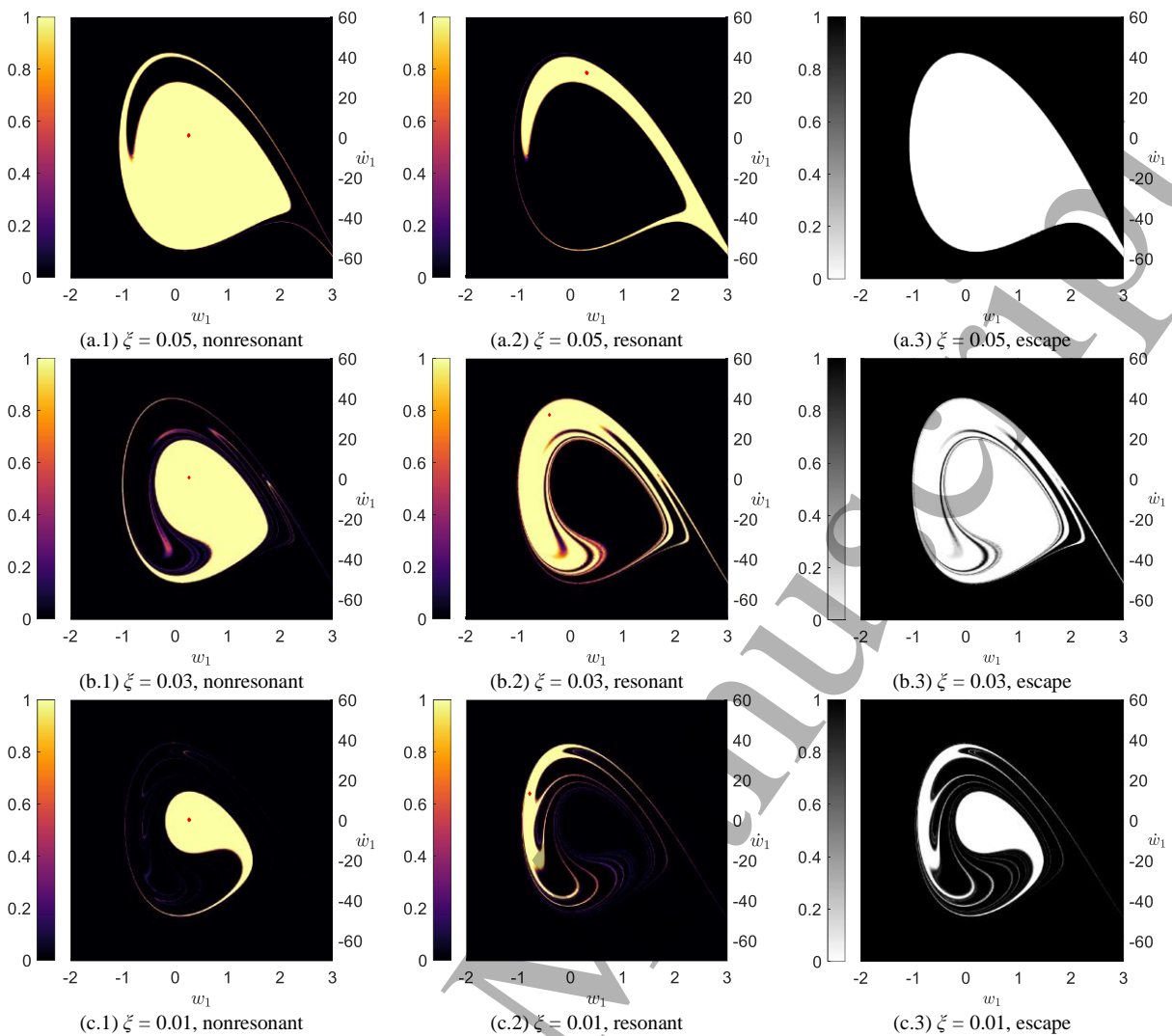

Figure 8. Resonance response curves of the reduced order model for $\xi = 0.01$ and varying amplitude *A*. Saddle-nodes in green, period-doubling points in red. – stable, -- unstable

Figure 9. Basins' distributions (color bar) dependency with the critical damping ratio ζ, for $A = 17$V and $\Omega = 15$. Attractors marked in red

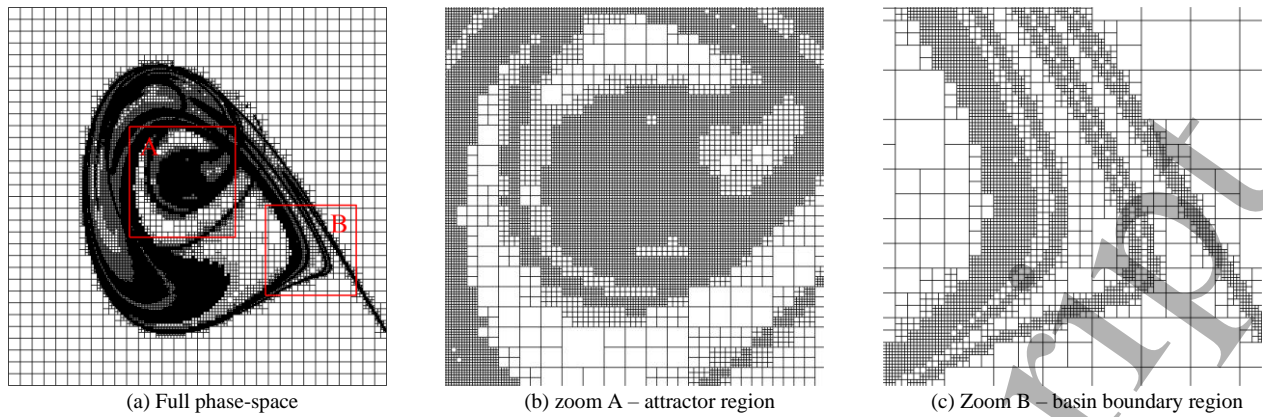| (a) Full phase-space | (b) zoom A – attractor region | (c) Zoom B – basin boundary region |

Figure 10. Example of phase-space adaptative discretization. Important regions are more refined, namely, attractors distributions and basins boundaries, while distant nonrelevant regions maintain a crude discretization. Zoomed regions depict the resolution contrast in (b) an attractor region and in (c) a basin boundary region
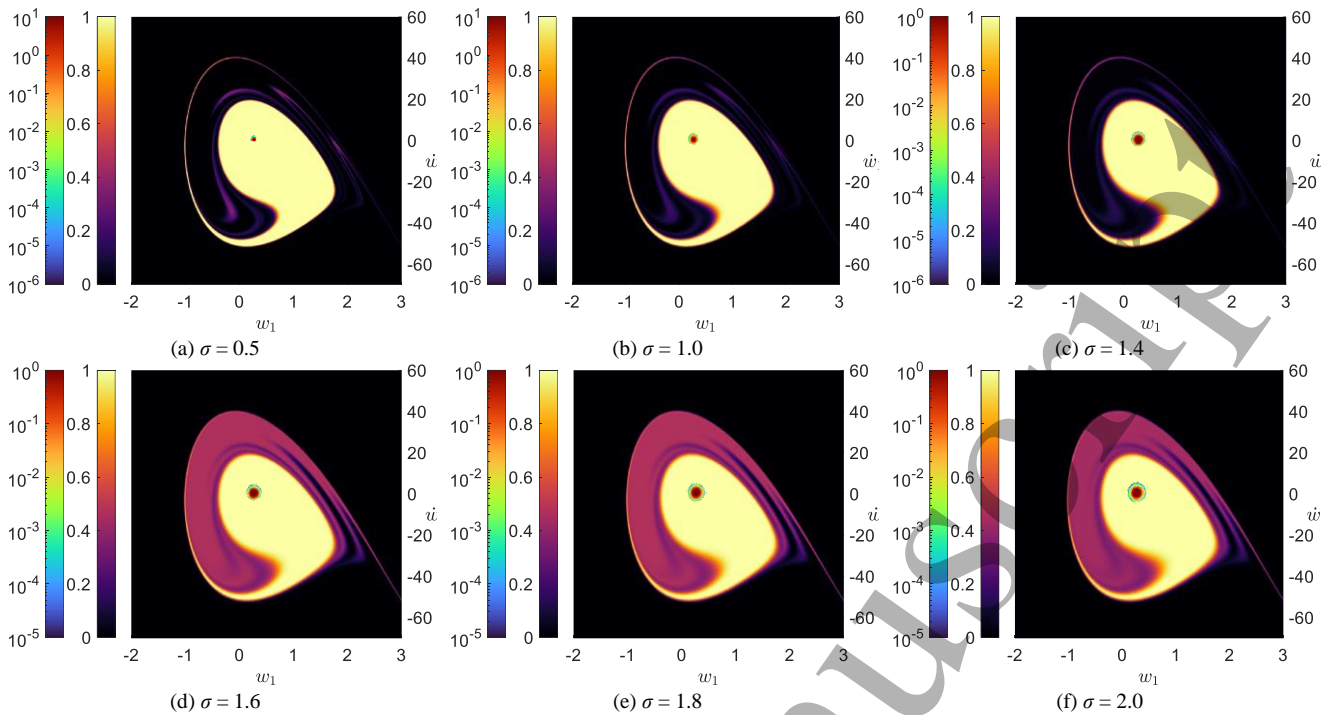
Benedetti *et al*

(a) $\sigma = 0.5$

(b) $\sigma = 1.0$

(c) $\sigma = 1.4$

(d) $\sigma = 1.6$

(e) $\sigma = 1.8$

(f) $\sigma = 2.0$

Figure 11. Stochastic nonresonant attractors' distributions (first color bar) and basins' distributions (second color bar) for varying noise intensity. $A = 17$V, $\Omega = 15$, $\xi = 0.03$
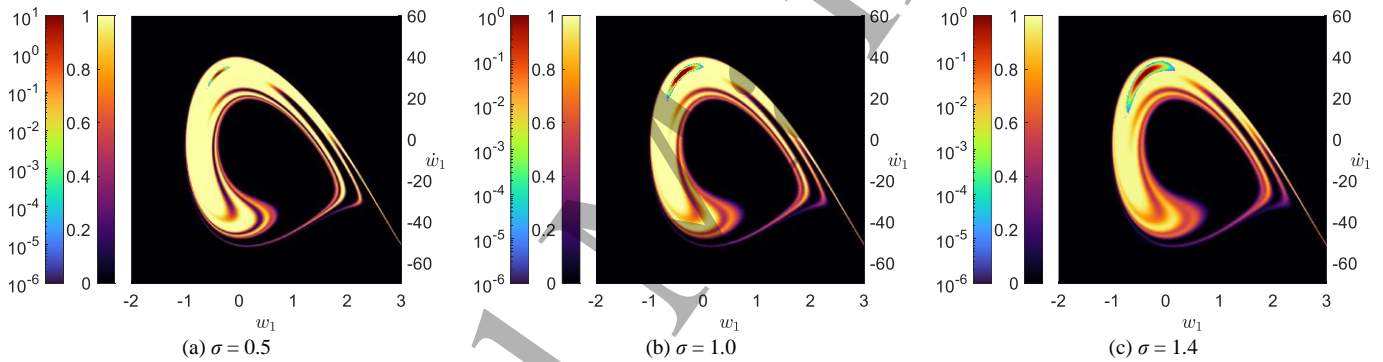

(a) $\sigma = 0.5$

(b) $\sigma = 1.0$

(c) $\sigma = 1.4$

Figure 12. Stochastic resonant attractors' distributions (first color bar) and basins' distributions (second color bar) for varying noise intensity. $A = 17$V, $\Omega = 15$, $\xi = 0.03$

(a) ε = 0.5   (b) ε = 1e-1   (c) ε = 1e-2

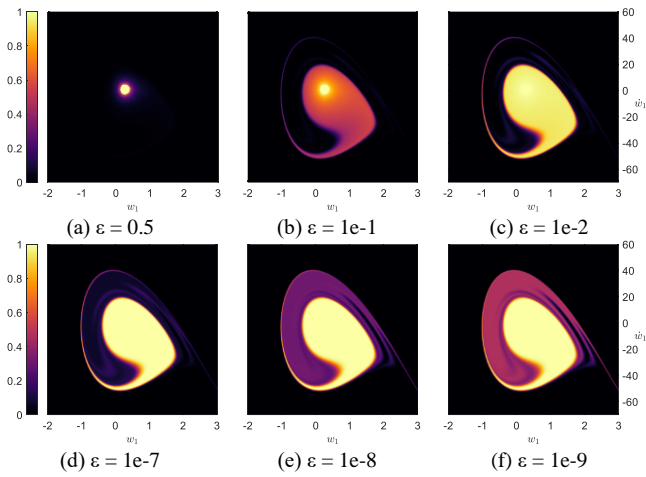(d) ε = 1e-7   (e) ε = 1e-8   (f) ε = 1e-9

Figure 13. Dependency of the nonresonant basin's distributions (color bar) with the time-horizon $1/\varepsilon$. $A = 17V$, $\Omega = 15$, $\xi = 0.03$, $\sigma = 1.6$
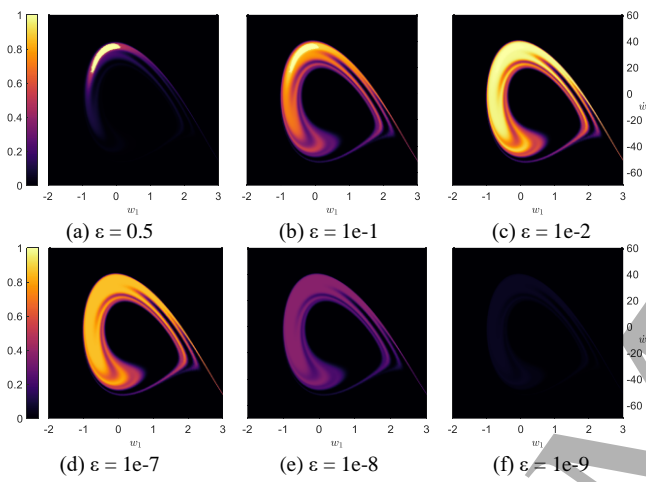

(a) ε = 0.5   (b) ε = 1e-1   (c) ε = 1e-2

(d) ε = 1e-7   (e) ε = 1e-8   (f) ε = 1e-9

Figure 14. Dependency of the resonant region's distribution (color bar) with the time-horizon $1/\varepsilon$. $A = 17V$, $\Omega = 15$, $\xi = 0.03$, $\sigma = 1.6$
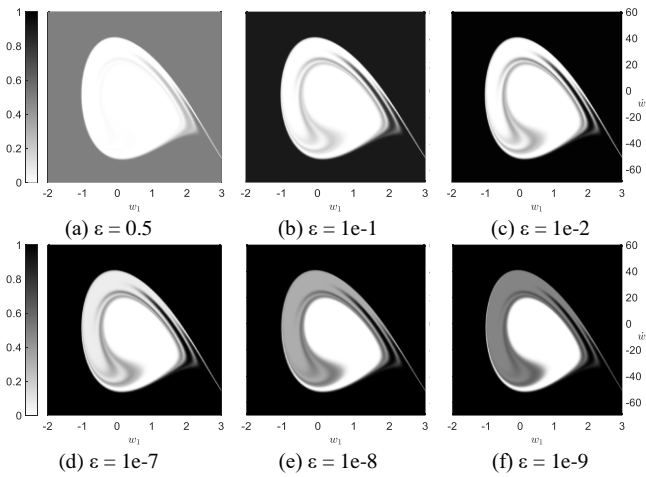
Benedetti *et al*

(a) ε = 0.5   (b) ε = 1e-1   (c) ε = 1e-2

(d) ε = 1e-7   (e) ε = 1e-8   (f) ε = 1e-9

Figure 15. Dependency of the escape region's distributions (color bar) with the time-horizon $1/\varepsilon$. $A = 17$V, $\Omega = 15$, $\xi = 0.03$, $\sigma = 1.6$
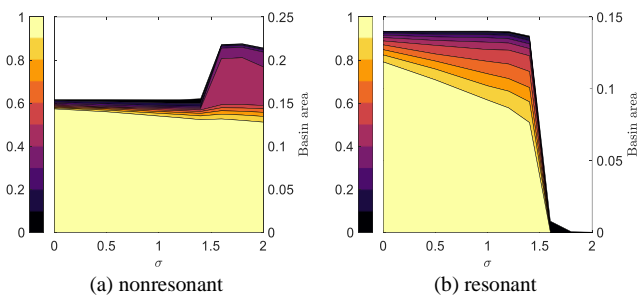

(a) nonresonant   (b) resonant

Figure 16. Integrity profiles of the weighted basins area as a function of the noise intensity σ for $A = 17$V, $\Omega = 15$, $\xi = 0.03$. Color scale corresponds to the probability threshold p. Time-horizon $1/\varepsilon = 1e9$
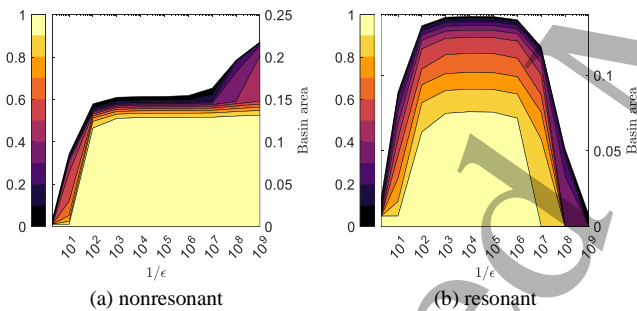

(a) nonresonant   (b) resonant

Figure 17. Integrity profiles of the weighted basins area as a function of the time-horizon $1/\varepsilon$ for $A = 17$V, $\Omega = 15$, $\xi = 0.03$, $\sigma = 1.6$. Color scale corresponds to the probability threshold p

(a.1) nonresonant, $\xi \sim U(0.04,0.05)$

(a.2) resonant, $\xi \sim U(0.04,0.05)$

(a.3) escape, $\xi \sim U(0.04,0.05)$

(b.1) nonresonant, $\xi \sim U(0.03,0.05)$

(b.2) resonant, $\xi \sim U(0.03,0.05)$

(b.3) escape, $\xi \sim U(0.03,0.05)$

(c.1) nonresonant, $\xi \sim U(0.02,0.05)$

(c.2) resonant, $\xi \sim U(0.02,0.05)$

(c.3) escape, $\xi \sim U(0.02,0.05)$

(d.1) nonresonant, $\xi \sim U(0.01,0.05)$

(d.2) resonant, $\xi \sim U(0.01,0.05)$
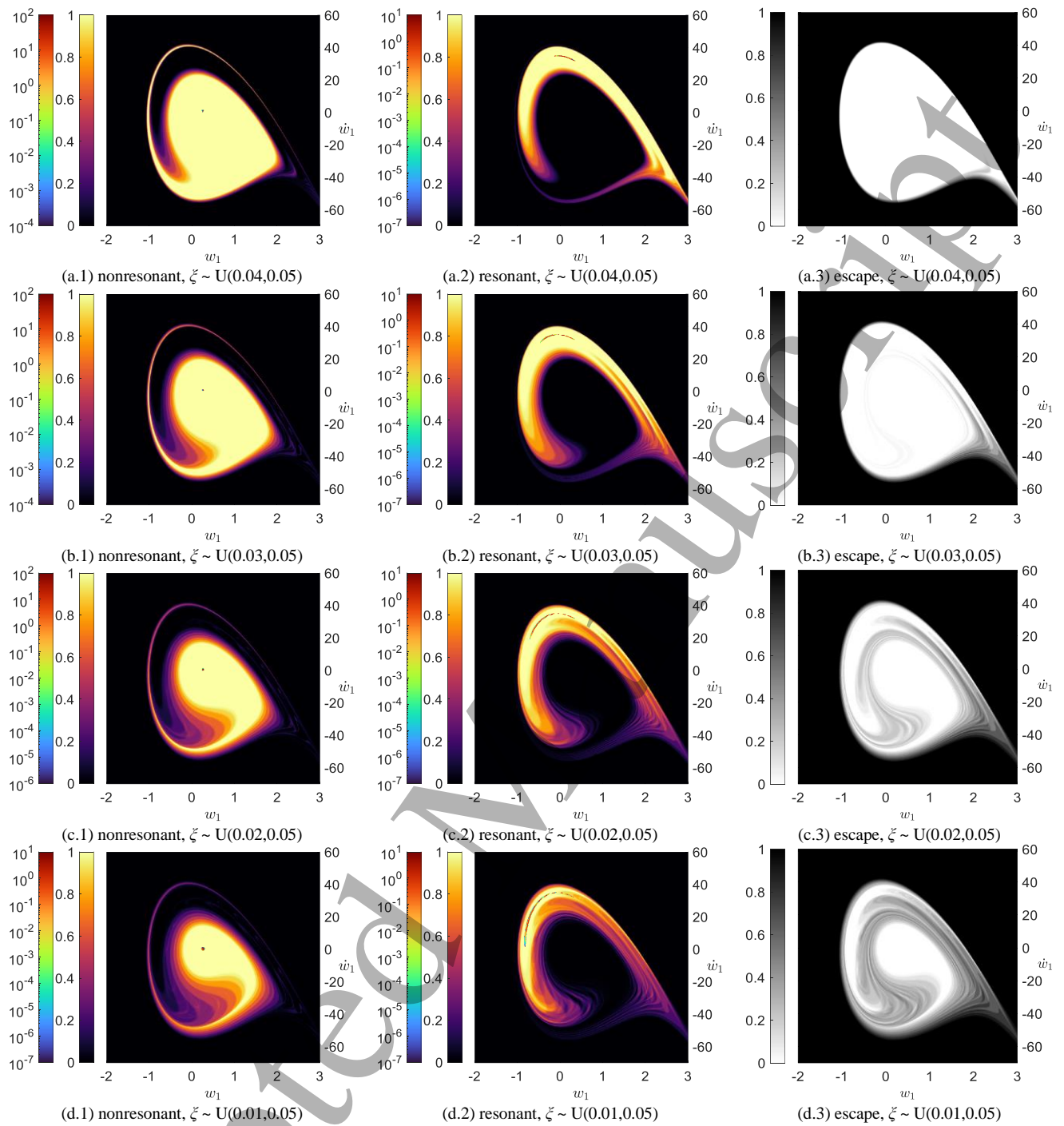
(d.3) escape, $\xi \sim U(0.01,0.05)$

Figure 18. Mean attractors' (first color bar), mean basins' (second color bar), and mean espace regions' (grey) distributions for varying damping ratio ξ distributions. $A = 17V$, $\Omega = 15$
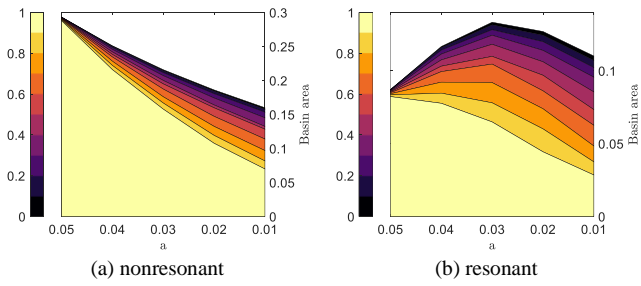
Benedetti *et al*

Figure 19. Integrity profiles of the weighted basins area as a function of the lower parameter uncertainty boundary *a* for $A = 17V$, $\Omega = 15$. Color scale corresponds to the probability threshold *p*